Effect of subgrid-scale mixing on the evolution of forced submesoscale instabilities

Sanjiv Ramachandran [a,*], Amit Tandon [a,b], Amala Mahadevan [c]

[a] Department of Physics, University of Massachusetts, Dartmouth, MA, United States
[b] Physics/School of Marine Sciences, University of Massachusetts, Dartmouth, MA, United States
[c] Woods Hole Oceanographic Institution, Woods Hole, MA, United States

ABSTRACT

We study the effect of subgrid-scale (SGS) mixing on the evolution of a density front initially in thermal-wind balance with a meridional density gradient and forced by downfront surface winds. The horizontal size of the model domain (O(100 km)) is large enough to contain mesoscale eddies while the horizontal grid resolution (500 m) is fine enough to resolve submesoscale eddies. The twin goals of this study are: (i) to determine what is a realistic level of SGS dissipation; and (ii) to explore the sensitivity of the resolved-scale dynamics to the SGS dissipation. To this end, we effect different levels of SGS dissipation using two SGS models: (i) constant lateral SGS viscosities (1 m^2 s^{-1} and 5 m^2 s^{-1}) and an analytically prescribed vertical SGS viscosity; and (ii) an existing anisotropic Smagorinsky model (ASM) developed for anisotropic grids with large aspect ratios between the horizontal and the vertical directions. An analysis of the eddy kinetic energy (EKE) budgets shows the surface stress boundary condition constrains all simulations to yield realistic values of SGS dissipation in a near-surface layer that is shear-driven and similar to the traditional Monin–Obukhov layer. Deeper down within the mixed layer, the EKE budget is buoyancy-driven with a more complicated balance that varies considerably among the different simulations. The simulations with constant K_x predict the buoyant generation of EKE is balanced almost solely by pressure transport with negligible local destruction, which gives rise to waves near the front. Recent observations near fronts show enhanced levels of irreversible destruction. The simulations with the ASM predict EKE budgets where both local destruction—through SGS dissipation—and pressure transport are part of the EKE balance.

The results obtained using the constant-K_x simulations suggest both horizontal and vertical SGS parameterizations have important effects on the resolved-scale dynamics. The simulations with $K_x = 5m^2 s^{-1}$ yield the most unrealistic results partly because the lateral viscosity is high enough to directly influence the instability scale. Yet the observed differences among the constant-K_x simulations are sometimes subtle and cannot be explained trivially by comparing K_x alone. For fixed K_x, we find simulations can exhibit higher spectral levels and stronger cascades (forward and inverse) upon increasing the vertical SGS viscosity. This suggests the sensitivity of submesoscale-resolving simulations to the vertical SGS parameterization needs to be better explored.

© 2013 Elsevier Ltd. All rights reserved.

1. Introduction

In the ocean, submesoscales are scales of motion smaller than the Rossby radius of deformation but large enough to be influenced by planetary rotation (Thomas et al., 2007). Numerical studies show oceanic density-fronts are active sites of submesoscale instabilities (Capet et al., 2008c,a,b; Fox-Kemper et al., 2008; Klein et al., 2008; Mahadevan, 2006; Mahadevan and Tandon, 2006) which occur in strongly frontogenetic regions associated with O(1) Rossby number (Ro), thereby creating conditions suitable for departure

from balanced dynamics (Molemaker et al., 2010; Molemaker and McWilliams, 2005). The O(1) Ro implies the dynamics at the submesoscales is not amenable to classical quasi-geostrophic (QG) analysis which assumes Ro ≪ 1 (Pedlosky, 1987).

A case study considered often in the literature and in some of the studies cited above is the evolution of a density front forced by downfront surface winds, which create loss of balance by destroying potential vorticity (PV) near the surface (Thomas, 2005) (Downfront winds are winds aligned with the frontal jet in thermal-wind balance with the lateral density gradient). In simulations such systems spawn submesoscale motions with O(100 m/day) vertical velocities at the frontal edges (Mahadevan, 2006). Such rapid vertical motions can accomplish the transport of nutrients from the ocean interior to the surface on inertial time-scales

and thus, could be an important factor governing phytoplankton production in the upper ocean (Lévi et al., 2001; Mahadevan and Archer, 2000).

Submesoscales have been conjectured to play an important role in the downscale transfer of energy from the O(100 km) mesoscales to scales O(0.1–100 m) associated with three-dimensional isotropic turbulence (Muller et al., 2005). This hypothesis has received support from simulations (Capet et al., 2008c) which show an onset of a forward cascade within the submesoscales. The mesoscales exhibit an inverse cascade of energy, on average, consistent with the quasi-geostrophic (QG) framework (Charney, 1971; McWilliams et al., 1994) while small-scale turbulence exhibits a forward cascade of energy, on average (Tennekes and Lumley, 1972). Submesoscale instabilities, by enabling forward cascades of energy in localized regions of unbalanced dynamics, can thus create pathways for the local removal of mesoscale energy in the ocean interior (Capet et al., 2008b; McWilliams, 2003), away from the boundaries.

Theory and numerical experiments (Boccaletti et al., 2007; Fox-Kemper et al., 2008) show submesoscale baroclinic instabilities significantly enhance the rate of restratification of the mixed layer (ML), implying one-dimensional mixing parameterizations, which neglect lateral processes, might fare poorly near density fronts. The stratification due to these instabilities can be an order of magnitude larger than that due to geostrophic adjustment alone (Mahadevan et al., 2010; Tandon and Garrett, 1994).

Past numerical studies of oceanic submesoscales can be divided crudely into one of two categories: (i) Simulations in computational domains that contain and resolve both mesoscale and submesoscale features, but are too coarse to resolve the smaller, turbulent scales;[1] and (ii) Large-eddy simulations (LES) in smaller domains with grid resolutions fine enough to resolve the turbulent scales. The former category is suitable for studying the evolution and coupling of meso- and submeso-scales whereas the latter is ideal for identifying mechanisms that trigger a forward cascade of energy to the smaller, isotropic scales associated with three-dimensional turbulent mixing. In the first category are studies by Mahadevan (2006), Mahadevan and Tandon (2006), Thomas et al. (2007), Capet et al. (2008c,a,b), Fox-Kemper et al. (2008) and Klein et al. (2008). These authors employed domains that are O(100 km) in the horizontal and O(100 m–1 km) in the vertical with corresponding grid resolutions of O(500 m–1 km), and O(1–10 m),[2] respectively. Our present study belongs in this category. The second category includes LES by Ozgokmen et al. (2011), Skyllingstad and Samelson (2012), Taylor and Ferrari (2009) and Taylor and Ferrari (2010) among others. These authors use domains that are O(1–10 km) in the horizontal and O(100 m) in the vertical with isotropic grids having O(1 m) resolution. The LES studies have grid resolutions fine enough to resolve three-dimensional turbulent motions and some of them (Skyllingstad and Samelson, 2012) use domains large enough to contain a 6 km baroclinic eddy. Both classes of simulations described above are different from the so-called MOLES (Fox-Kemper and Menemenlis, 2008), or Mesoscale Ocean Large-Eddy Simulations, where the grid resolution is fine enough to resolve the mesoscale kinetic energy spectrum but too coarse to resolve submesoscales. In MOLES, the grid-scale is associated with a direct potential enstrophy cascade but not with a forward cascade of energy. In submesoscale-resolving simulations the average spectral flux of energy switches from an inverse to forward cascade at scales O(1–10 km) (Capet et al., 2008b), that are larger than the grid-scale (Capet et al., 2008b; Klein et al., 2008). Thus, such simulations—un-like MOLES—might be compatible with traditional LES subgrid-scale (SGS) closures which typically (but not always) are designed to ensure a net forward cascade of energy from the resolved to the subgrid scales of motion.

1.1. LES versus RANS subgrid-scale models

In LES subgrid closures the subgrid length scale is modelled as proportional to the grid spacing. In RANS (Reynolds Averaged Navier–Stokes; Launder et al., 1975) modelling the subgrid length scale must be parameterized as the grid spacing is too coarse to be a physically relevant length scale for the subgrid motions. It follows the SGS viscosity and diffusivity move in lockstep with the grid spacing in LES but not in RANS closures like the K-Profile Parameterization (KPP; Large et al., 1994) or the k-ϵ family of models (Pope, 2000), for instance. An SGS model has two distinct functions: (i) parameterization of the SGS stresses (or fluxes); and (ii) dissipation of the resolved scales. In well-resolved LES the subgrid terms are of leading order in the balance of the resolved-scale kinetic energy but not in that of resolved-scale momentum. The details of the modelled SGS stresses (and fluxes) are of secondary importance to the ability of the SGS model to dissipate the large eddies in a realistic manner. Thus, modelled SGS stresses that correlate poorly with DNS fields can nevertheless be tuned to extract energy from the resolved scales in a physically consistent manner (Reynolds, 1990). In RANS the turbulence resides entirely at the subgrid scales with none of it resolved by the grid. The subgrid divergence terms are, therefore, of leading order in the evolution of the resolved-scale momentum field which places additional demands on the SGS closure, namely, that of parameterizing the unresolved scales accurately as they now account for a significant fraction of the total turbulent stresses. The two functions of the SGS model are now intertwined and cannot be addressed in isolation. We emphasize parameterizing the SGS stresses accurately is a concern to the extent it is *necessary* to achieve realistic SGS dissipation. A focus on the former for its own sake is of questionable value as there exist SGS models that dissipate insufficiently in simulations in spite of encouraging correlations with DNS fields in offline tests.[3]

In principle, increasing the resolution progressively warrants a move away from RANS closures toward LES closures but a sharp transition between these two regimes is unlikely (Wyngaard, 2004). The issue of LES versus RANS is complicated further when various factors, such as, strong stratification, solid surfaces, etc. limit the eddy length scale to scales finer than the grid resolution leading to RANS-like conditions in select regions of the flow even at resolutions typical of LES (Sullivan et al., 1994). The engineering community has long wrestled with the LES–RANS dichotomy within the context of "Hybrid LES" (Spalart et al., 1997; Speziale, 1998) and Detached Eddy Simulation (DES; Spalart, 2009) methods which, broadly speaking, advocate switching between RANS and LES based on the flow physics. For instance, many hybrid LES methods use a RANS model near a solid surface and an LES solution away from it, matching the two solutions across the LES–RANS interface. Other studies (Perot and Gadebusch, 2009) have adopted a different approach by questioning the very basis for the LES–RANS dichotomy and arguing RANS closures can perform consistently at any resolution. The above arguments give an indication of some of the challenges involved in developing reliable subgrid models at resolutions nestled in between the LES and RANS

---

[1] These are sometimes referred to as SMOLES (Submesoscale & Mesoscale Ocean Large-Eddy Simulation.)

[2] This refers to the near-surface vertical resolution as these studies typically use a vertically stretched grid.

[3] In offline or *a priori* testing we construct the SGS fields by filtering DNS or measured fields down to the appropriate scale. No simulations using the SGS model being assessed are necessary for this mode of testing. Assessing an SGS model based on its real-time performance in a simulation, as in the present study, is referred to as *a posteriori* testing.

regimes. To what extent do these issues bear on meso- and sub-meso-resolving simulations? Answering this question will require more studies targeted specifically at exploring resolved-subgrid interactions as a function of grid spacing. A recent example of a study with similar, but not identical, goals is the investigation of submesoscale dynamics in tropical instability waves of the Pacific ocean using a series of simulations at different resolutions (Marchesiello et al., 2011). The simulations explicitly set lateral SGS mixing to zero and use the KPP scheme for vertical SGS mixing. They found the effects of numerical mixing are significant at wavenumbers well below the grid-cutoff wavenumber which implies the effective resolution of the simulation is lesser than that allowed by the grid. The effective resolution could depend potentially on the SGS model as well, through its dissipation characteristics.

1.2. Motivation of this study

The previous discussion raises several concerns, of which we now list a few we believe are important:

1. How sensitive are the resolved-scale features in meso- and sub-meso-resolving simulations to the level of SGS dissipation? Is it possible to determine what is an appropriate level of SGS dissipation?
2. For a given level of SGS dissipation, which family of SGS closures yields better resolved-scale statistics? LES or RANS?
3. Given an SGS dissipation level and a class of SGS closures (LES or RANS) which SGS closures within that class yield better resolved-scale statistics? Are there common features that characterize the closures that yield superior results?

The first of these questions is the focus of the present study. In the manner posed, each question is a logical extension to its predecessor and the insights gained from one will help answering the other. Our emphasis on SGS dissipation follows from the arguments outlined earlier. We use a small set of closures to effect different levels of SGS dissipation: (i) an LES subgrid closure, the anisotropic Smagorinsky model (ASM; Roman et al., 2010); and (ii) constant lateral SGS viscosities with an analytically prescribed vertical SGS viscosity. A wider selection of SGS models is unnecessary for our stated goals as we demonstrate in the course of this paper. We simulate a baroclinic front confined to the mixed layer and forced by downfront winds, a set-up common to some of the numerical studies cited earlier. The downfront winds aid in propping up the front by Ekman advection of heavier over lighter water while the submesoscale instabilities relax the front by extracting the reservoir of available potential energy in the front. The combined effect of these two competing forces will determine whether there is net destratification, net restratification or a dynamic equilibrium between these two mechanisms (Mahadevan et al., 2010).

We use the Process Study Ocean Model (PSOM, Mahadevan, 2006), a three-dimensional, non-hydrostatic, Boussinessq model for all simulations. Our choice of the ASM for the LES subgrid closure is motivated by its simplicity and ease of implementation. The Smagorinsky model (SM; Smagorinsky, 1963; Lilly, 1967) and its subsequent variants are arguably the most basic of LES subgrid closures. An earlier study (Fox-Kemper et al., 2008) used a Smagorinsky SGS model to parameterize lateral SGS mixing in conjunction with a constant background vertical SGS viscosity. They explicitly set the SGS diffusivity to zero. The ASM prescribes both lateral and vertical SGS viscosities (and diffusivities). Furthermore, it accommodates anisotropic grids and hence is suitable for our simulations where the horizontal grid resolution is much coarser than the vertical grid resolution.

Some comments about the nature of our intended comparison are in order. In a trivial sense it is evident two simulations with different SGS dissipation will evolve differently. Less evident is which features of the resolved-scale flow evolve differently and whether the observed differences are critical enough to merit our attention. While comparing the various simulations we highlight those differences that are central to the evolution of the submesoscale instabilities. Where possible, we look for common causes underlying these differences. Evaluating the performance of an SGS model is easier when either DNS, measurements or theory provide reliable benchmarks against which the model results can then be assessed. An example of such an instance is well-resolved LES of 3D turbulence where the grid spacing resolves the inertial-subrange. Under such conditions Kolmogorov's universal scaling for the inertial-subrange spectra, validated by extensive DNS and experimental evidence, predicts the "correct" level of dissipation an SGS model must achieve and tuning the SGS model accordingly is a straightforward exercise. We presently lack similar scaling arguments when the grid spacing lies within the submesoscales, from either theory or measurements. The O(100 km) size of our proposed computational domains implies DNS is unfeasible. Comparisons with DNS of smaller domains that do not contain the mesoscales are of limited value as the straining of the density field by the larger mesoscale eddies is an essential ingredient for the "mesoscale to submesoscale transition" (Capet et al., 2008c). In the absence of existing guidelines for the optimal level of SGS dissipation, we use the eddy kinetic energy budgets to estimate physically meaningful levels for the SGS dissipation under quasi-equilibrium conditions where the restratification and destratification tendencies counter each other approximately. Such an estimate is useful inasmuch as it offers an order of magnitude for the SGS dissipation and can be computed using the large-scale parameters of the simulation.

1.3. Outline

In Sections 2.1 and 2.2 we describe the model equations in PSOM and the SGS model, respectively. Section 3 describes the initial conditions and the set-up of the numerical simulations. We discuss results in Section 4 and summarize our conclusions in Section 5.

2. Modelling

For notational ease we switch between the indexed and the conventional representation of variables when necessary. For instance, the symbols $\{x_i, (i = 1, 2, 3)\}$ and (x, y, z) are equivalent as are $\{u_i, (i = 1, 2, 3)\}$ and (u, v, w).

2.1. Model equations

The Process Study Ocean Model, or PSOM, is a three-dimensional (3D), non-hydrostatic model (Mahadevan, 2006) where the top layer of grid cells follows the free-surface. For the discretization, the code uses Quadratic Upstream Interpolation for Convective Kinematics (QUICK; Leonard, 1988), a scheme known for its negligible numerical diffusion and dispersion. A description of the model variables follows. Variables with the tilde operator represent filtered (resolved-scale) variables and those without the tilde operator represent unfiltered fields. We use the words resolved (or resolved-scale) and filtered interchangeably in this document. The unfiltered fields, in principle, contain information across the entire range of length scales down to the Kolmogorov microscale (Tennekes and Lumley, 1972). Only the filtered fields are available because a discrete computational grid cannot resolve scales of motion finer than the grid resolution. The nonlinearity of the advective term in the Navier–Stokes equations, however, gives

rise to subgrid-scale terms that need to be modelled to close the system of equations for the filtered variables.[4] The model equations in non-dimensional form are:

$$D_t \tilde{\rho} = \widetilde{F}^{\tilde{\rho}} - \frac{\partial \tau_i^{\rho}}{\partial x_i} \tag{1}$$

$$D_t \tilde{u} + Ro^{-1} \left(\tilde{p}_x + \gamma \tilde{q}_x^* - f \tilde{v} + Ro \delta b \tilde{w} \right) = \widetilde{F}^x - \frac{\partial \tau_{ij}^d}{\partial x_j}; \quad i = 1 \tag{2}$$

$$D_t \tilde{v} + Ro^{-1} \left(\tilde{p}_y + \gamma \tilde{q}_y^* + f \tilde{u} \right) = \widetilde{F}^y - \frac{\partial \tau_{ij}^d}{\partial x_j}; \quad i = 2 \tag{3}$$

$$D_t \tilde{w} + Ro^{-2} \delta^{-1} \left(\frac{\gamma}{\delta} \tilde{q}_z^* - b \tilde{u} \right) = \widetilde{F}^z - \frac{\partial \tau_{ij}^d}{\partial x_j}; \quad i = 3 \tag{4}$$

$$\tilde{u}_x + \tilde{v}_y + Ro \tilde{w}_z = 0, \tag{5}$$

where $D_t \equiv \partial_t + \tilde{u}\partial_x + \tilde{v}\partial_y + Ro\tilde{w}\partial_z$ is the non-dimensional material derivative operator. The variables $\tilde{u}$, $\tilde{v}$ and $\tilde{w}$ denote the non-dimensional filtered velocity components along the eastward (x), northward (y) and upward (z) directions, respectively, on the earth's surface. The variable $\tilde{\rho}$ denotes the filtered density perturbation from the background stratification prescribed at $t = 0$. The components of the Coriolis acceleration scaled with the earth's angular velocity, Ω, are denoted by $f = 2\sin(\phi)$ and $b = 2\cos(\phi)$ where ϕ is the latitude. Defining U, W, L and D to be the relevant scales for the horizontal velocity, vertical velocity, the horizontal and vertical length scales, respectively, the non-dimensional parameters in the model are: (i) the Rossby number, $Ro = U/\Omega L$, where Ω is the angular velocity of rotation of the earth; (ii) ratio of the non-hydrostatic (NH) to hydrostatic (HY) pressure variations, $\gamma = Q/P$, where Q and P are the characteristic scales for the NH and HY components, respectively; and (iii) the aspect ratio, $\delta = D/L$. For the NH runs, it is appropriate to set $\gamma = \delta$ (Mahadevan, 2006). The filtered HY component is denoted by $\tilde{p}$ and the filtered, modified NH component (discussed below) by $\tilde{q}^*$. Setting $\gamma = 0$ turns off the NH effects. By definition, $\tilde{p}$ satisfies $\tilde{p}_z + \tilde{\rho}g = 0$, where g is the acceleration due to gravity. Scaling the vertical vorticity equation and assuming a balance between the advection and divergence terms yields $W = Ro\delta U$ (Mahadevan, 1996).

The filtered forcing terms are shown on the right hand side of (1)–(4) as $\widetilde{F}^{\rho}, \widetilde{F}^x$ and so on. We assume implicitly the forcing terms are described completely by their filtered parts, i.e., they lack spatial structure finer than the grid resolution. The non-dimensional SGS density fluxes are denoted by $\tau_i^{\rho} = \widetilde{\rho u_i} - \tilde{\rho}\tilde{u}_i$. We denote the deviatoric non-dimensional SGS momentum stress tensor as $\tau_{ij}^d = \widetilde{u_i u_j} - \tilde{u}_i\tilde{u}_j - (2/3)\delta_{ij}e_{sgs}$, where δ_{ij} is the Kronecker-Delta operator and $e_{sgs} = \widetilde{u_i u_i} - \tilde{u}_i\tilde{u}_i$ is the non-dimensional SGS kinetic energy. By construction, τ_{ij}^d is traceless. The variable $\tilde{q}^*$ is the modified, filtered NH component of pressure as it includes a contribution from $(2/3)e_{sgs}$, in addition to the true NH pressure component. To solve for the filtered fields in (1)–(5), we must parameterize the three SGS fluxes and the six independent SGS stresses. Knowledge of the SGS kinetic energy requires an additional parameterization for e_{sgs}, which we do not undertake in this study.

2.2. Subgrid model

Before describing the ASM, we provide a brief discussion of the adaptation of the Smagorinsky model and some of its variants to LES of 3D turbulence. Lilly, 1967 first tuned the Smagorinsky sub-

grid model (SM; Smagorinsky, 1963) for LES of homogeneous, isotropic turbulence by constraining the SGS dissipation to yield the correct magnitude and slope of energy spectra within the inertial-subrange, in accordance with Kolmogorov scaling.[5] His derivation requires the grid-cutoff wavenumber to resolve the inertial-subrange. The value of the Smagorinsky model constant Lilly derived is not meant to be universal due to the assumptions underlying his derivation. For instance, it is not valid for strongly anisotropic turbulence or when the grid resolution is too coarse to resolve the inertial subrange. Germano et al. (1991) developed the Dynamic Smagorinsky model (DSM) which prescribes the subgrid model constant as a function of space and time by relating the resolved-scale fields filtered at two different scales through the Germano identity, defined in the same study. This dynamic evaluation of the subgrid model constant enables the DSM, in principle, to exhibit negative eddy-viscosities and thus, backscatter, or, the transfer of energy from the subgrid to the resolved scales. In practice, negative eddy-viscosities give rise to numerical instabilities (Lilly, 1992) and are usually clipped, effectively eliminating backscatter. Both DNS (Piomelli et al., 1991) and field measurements (Sullivan et al., 2003) of 3D turbulence show significant amounts of backscatter with a slightly stronger forward cascade to yield a net forward (downscale) cascade of energy. The SM, by construction, permits only a downscale transfer of energy from the resolved to the subgrid scales, at every single grid point. When the grid scale lies within the submesoscales, where the flow regime is considerably different from 3D, isotropic turbulence, it is unclear what are the relative fractions of grid-scale forward and inverse cascades, although simulations show the spectral flux of kinetic energy switches from an inverse to a forward cascade at scales O(10 km) (Capet et al., 2008b). The DSM model has been used successfully in past LES studies of oceanic flows (Ozgokmen et al., 2009; Ozgokmen et al., 2011; Tejada-Martínez, 2009) with nearly isotropic grids. Scotti and Meneveau, 1993; and modified the SM and the DSM, respectively, for anisotropic grids by obtaining analytical expressions for the subgrid model constant as a function of the grid anisotropy, assuming the grid spacing in all three directions resolves the inertial-subrange. Other anisotropic variants of the DSM include the formulation by Cottet and Wray, 1997 based on a leading order expansion for the Leonard term (Leonard, 1974) in the subgrid-scale tensor.

2.2.1. ASM

Simulations designed to study the simultaneous evolution of both mesoscale meanders and submesoscale features in the ocean require anisotropic grids, as the vertical resolution, Δz, is much finer than the horizontal resolution, Δx (or Δy), due to the large aspect ratio of the domains, with horizontal scales much larger than the vertical scales (Capet et al., 2008c; Klein et al., 2008; Mahadevan, 2006). Roman et al., 2010 developed an anisotropic Smagorinsky model (ASM) that derives from past work (Kamenkovich, 1977; Wajsowicz, 1993; Miles, 1994) and is designed for grids where $\Delta x \gg \Delta z$. Owing to the highly anisotropic grids and coarse resolutions[6] in our simulations, we use the SGS model designed by Roman et al., 2010. ASM does not require the grid resolution to belong in the inertial subrange, but this generality comes at a cost, namely, the lack of analytical expressions relating the subgrid model constants to the grid anisotropy. A short description of the formulation of the ASM follows.

Let us denote the dimensional eddy-viscosity tensor by K_{ij}, which is assumed to be symmetric. ASM reduces the six independent components to three: $K_{11} = K_{12} = K_{22}, K_{13} = K_{23}$ and K_{33}. In

---

[4] Except in a Direct Numerical Simulation (DNS) where the grid resolution is fine enough to resolve the Kolmogorov microscale, removing the need for an SGS model

[5] Corrsin, 1951 advanced equivalent arguments for an universal form of the passive scalar spectrum in isotropic turbulence.
[6] Insufficient to resolve the inertial subrange

the discussion below, we use upper-case symbols for dimensional variables. The three independent components are given by:

$$K_{11} = (c_1 \Delta x)^2 |\widetilde{S}_h|; \quad K_{13} = (c_2 \Delta z)^2 |\widetilde{S}_v|; \quad K_{33} = (c_3 \Delta z)^2 |\widetilde{S}_r|, \quad (6)$$

where the dimensional, filtered strain rates $\widetilde{S}_h, \widetilde{S}_v$ and $\widetilde{S}_r$ are defined as follows:

$$|\widetilde{S}_h| = \sqrt{2\left(\widetilde{S}_{11}^2 + \widetilde{S}_{22}^2 + \widetilde{S}_{12}^2\right)} \quad (7)$$

$$|\widetilde{S}_v| = \sqrt{4\widetilde{S}_{13}^2 + 4\widetilde{S}_{23}^2} \quad (8)$$

$$|\widetilde{S}_r| = \sqrt{2\widetilde{S}_{33}^2}. \quad (9)$$

In (7)–(9) the filtered strain-rate tensor $\widetilde{S}_{ij} = 0.5\left(\partial \widetilde{U}_i/\partial \widetilde{X}_j + \partial \widetilde{U}_j/\partial \widetilde{X}_i\right)$ where $\widetilde{U}_i$ is the dimensional ith component of velocity and $\widetilde{X}_i$ is the dimensional ith coordinate. The stress divergence terms in the dimensional horizontal momentum equations are (Roman et al., 2010),

$$\frac{\partial}{\partial \widetilde{X}_1}\left(2K_h\widetilde{S}_{i1}\right) + \frac{\partial}{\partial \widetilde{X}_2}\left(2K_h\widetilde{S}_{i2}\right) + \frac{\partial}{\partial \widetilde{X}_3}\left(2K_v\widetilde{S}_{i3}\right); \quad i = 1, 2, \quad (10)$$

where $K_h = K_{11}$ and $K_v = K_{13}$. The stress divergence terms in the dimensional vertical momentum equation are,

$$\frac{\partial}{\partial \widetilde{X}_1}\left(2K_v\widetilde{S}_{i1}\right) + \frac{\partial}{\partial \widetilde{X}_2}\left(2K_v\widetilde{S}_{i2}\right) + \frac{\partial}{\partial \widetilde{X}_3}\left(2K_r\widetilde{S}_{i3}\right); \quad i = 3, \quad (11)$$

where $K_r = K_{11} - 2K_{13} + 2K_{33}$ (Roman et al., 2010). The eddy-diffusivities, K_i^ρ, are computed assuming a constant eddy Prandtl number, Pr_e, such that the horizontal components $K_1^\rho = K_2^\rho = Pr_e^{-1}K_h$ and the vertical component $K_3^\rho = Pr_e^{-1}K_v$. The constant-Pr_e assumption is one of convenience and lacks a rigorous basis (Moeng and Wyngaard, 1988) but is invoked frequently in LES studies due to its simplicity (Harcourt and D'Asaro, 2008; Sullivan et al., 2007; Taylor and Ferrari, 2010). Roman et al., 2010 use $Pr_e = 0.5$, while some LES studies use a value of 1 (Harcourt and D'Asaro, 2008; Taylor and Ferrari, 2010). We will assume $Pr_e = 1$ in all our simulations. For the value of Ro used in our simulations (discussed in Section 3) the third term in (11) scales as an order of magnitude smaller than the other two terms in the equation. Hence, to simplify our subgrid parameter space, we further impose $c_2 = c_3$ in all our runs, that leaves two free SGS parameters, c_1 and c_2

We modify the ASM slightly in our simulations. In the formulation by Roman et al., 2010 there is no dependence on the Richardson number, Ri, in (6) which implies vertical mixing (of momentum or density) regardless of the underlying stratification. To suppress such unphysical mixing Ozgokmen et al., 2007 multiplied the vertical components of the eddy-viscosity and/or eddy-diffusivity by the following function (Ozgokmen et al., 2007):

$$f(Ri) = \begin{cases} 1 & Ri < 0 \\ \sqrt{1 - \frac{Ri}{Ri_c}} & 0 \leqslant Ri \leqslant Ri_c = 0.25 \\ 0 & Ri > Ri_c. \end{cases} \quad (12)$$

The function in (12) turns off the vertical mixing when Ri exceeds a critical value, $Ri_c = 0.25$, above which the stratification is considered too strong to sustain continuous turbulence. The correction factor in (12) is empirical and neglects patchy, intermittent mixing for $Ri_c > 0.25$ (Ohya et al., 2008). Ozgokmen et al., 2007 found the Ri-based correction works best when it is applied only to the vertical SGS diffusivity but not to the vertical SGS viscosity. Thus, we restrict the use of the correction factor in (12) to K_ρ. The threshold value of $Ri_c = 0.25$ is perhaps more suitable for high-resolution LES capable of resolving Kelvin–Helmholtz instabilities. We confirmed increasing Ri_c to 1 does not alter the results significantly as the onset of submesoscale instabilities causes Ri to attain O(1) values rapidly after 5–6 days in the simulation.

Table 1
Description of runs using constant lateral SGS viscosities (K_x, K_y) and an analytically prescribed vertical SGS viscosity (K_z). The prescribed K_z profile is a hyperbolic tangent.

Run	$K_x = K_y$ (m^2 s^{-1})	K_z (m^{2}s^{-1}) Interior: 1×10^{-5}
KX1KZ1	1	Ekman layer: 1×10^{-3}
KX1KZ4	1	Ekman layer: 4×10^{-3}
KX5KZ1	5	Ekman layer: 1×10^{-3}
KX5KZ4	5	Ekman layer: 4×10^{-3}

2.2.2. Constant SGS lateral viscosities

Table 1 shows the four different combinations of constant lateral SGS viscosities (K_x, K_y) and analytically prescribed vertical SGS viscosity (K_v) profiles used in our simulations. These runs supplement those with the ASM and serve to make clearer the influence of SGS dissipation on the resolved-scale statistics.

In simulations with the ASM we found the lateral viscosity attains localized maximum values ≈ 5 m^2 s^{-1} along the frontal meanders whereas its zonally-averaged mean values are ≈ 1 m^2 s^{-1} near the surface. Accordingly, the values $K_x = 1$ m^2 s^{-1} and $K_x = 5$ m^2 s^{-1} are meant to mimic the ASM crudely in its mean and instantaneous lateral dissipation characteristics. For each of these K_x values we use two vertical SGS viscosity (K_v) profiles varying smoothly from 10^{-5} m^2 s^{-1} in the interior to either 10^{-3} m^2 s^{-1} or 4×10^{-3} m^2 s^{-1} within the Ekman layer (depth= $(0.4/f)(\tau_x/\rho_0)^{1/2}; \tau_x \equiv$ Zonal wind stress).[7] Our choice of K_v within the Ekman layer is also guided partly by the corresponding values predicted by the ASM. Within the set of constant K_x simulations, the four combinations in Table 1 allow us to isolate the effects of horizontal and vertical contributions to the SGS dissipation.

3. Numerical experiments

In Table 2 we list the physical parameters in our numerical simulations which follow those in the study by Mahadevan (2006).

3.1. Lateral grid resolution

The lateral grid resolution resolves the most unstable mode predicted by Stone's analysis of ageostrophic baroclinic instabilities (Stone, 1970). For representative values of $U = 0.1$ m s^{-1}, $f = 10^{-4}$ s^{-1} and $Ri = 1$, his analysis estimates the wavelength of the most unstable mode as $(2\pi U/f)\sqrt{5(1 + Ri)/2}$, or 5.6 km, which is an order of magnitude larger than Δx. The grid resolution is too coarse to resolve length scales associated with symmetric instability (Taylor and Ferrari, 2009, 2010) but vertical profiles of the balanced Richardson number, Ri_g, averaged near the front indicate a rapid increase to values greater than 1 after the onset of instabilities ($\approx 5T_f$) implying the conditions necessary for symmetric instability ($0.25 < Ri_g < 0.95$) are violated soon thereafter. Hence, the role of symmetric instability in our simulations is likely confined to the first few inertial periods.

We show results only for $\Delta x = 500$ m but confirmed simulations with $\Delta x = 750$ m and $\Delta x = 1000$ m reproduce the trends observed here. We do not expect our results to hold for arbitrarily coarse lateral grid resolutions because the grid spacing needs to resolve the onset of the forward cascade reported in past studies. Failing that, the use of an LES-based SGS model that ensures a net forward cascade is questionable.

---

[7] This implies K_v would assume the background value everywhere in the domain in the absence of surface winds.

Table 2
Non-dimensional and dimensional simulation parameters.

Description	Symbol	Value
Non-dimensional parameters		
Aspect ratio	δ	10^{-2}
Rossby number	Ro	0.1
Ratio of non-hydrostatic to hydrostatic pressure	γ	$= \delta$
Dimensional parameters		
Time step	Δt	216 s
Domain size (zonal)	L_x	96 km
Domain size (meridional)	L_y	192 km
Domain size (vertical)	L_z	500 m
Grid resolution (zonal)	Δx	500 m
Grid resolution (meridional)	Δy	500 m
Grid resolution (vertical)	Δz	3.6 m (near-surface)
		35 m (bottom)
Westerly wind stress	τ_x	0.1 N m^{-2} (amplitude)
Coriolis parameter	f_0	10^{-4} s^{-1}
Bottom friction coefficient	r_{bot}	5×10^{-4} s^{-1}
Mixed layer depth	MLD	105 m (Initial value)
Peak lateral buoyancy gradient	$\partial b/\partial y$	0.9×10^{-7} s^{-2} (Initial value)

3.2. Damping of the most unstable mode for $K_x = 5\ m^2\ s^{-1}$

Assuming a linear framework, a viscosity of 5 m^2 s^{-1} will damp the unstable mode over a timescale $1/(\kappa \times 5)^2$ s, where $\kappa = 2\pi/(5.6 \times 10^3)$ rad m^{-1}. The above calculation yields a damping timescale ≈ 2 days which suggests a viscosity of $K_x = 5$ m^2 s^{-1} could influence directly the instability scale as submesoscale instabilities evolve on inertial timescales. We nevertheless include the simulations with $K_x = 5$ m^2 s^{-1} as they are necessary to quantify the differences between the two sets of simulations ($K_x = 1$ m^2 s^{-1} and $K_x = 5$ m^2 s^{-1}). Moreover, the above estimate omits the influence of vertical SGS mixing which, we show, has an important role to play.

3.3. Boundary conditions

The boundary conditions are periodic in the zonal direction. The southern and northern boundaries are impermeable walls across which we impose zero advective fluxes and zero meridional gradients of the velocity, density and, SGS fields. The topmost layer of grid cells follow the free-surface (Mahadevan, 1996). The SGS

stresses τ_{13}^d and τ_{23}^d at the free-surface satisfy $\tau_x/\rho_0 = \tau_{13}^d$ and $\tau_y/\rho_0 = \tau_{23}^d$, where τ_y is the meridional surface wind-stress (zero in this study) and $\rho_0 = 1027$ kg m^{-3} is the reference density. The SGS flux τ_3^ρ at the surface is set equal to the surface density flux, which in this study is zero due to the absence of cooling or heating at the surface. We model bottom friction using a linear drag, $r_{bot}(U, V)$, where the constant bottom friction coefficient $r_{bot} = 5 \times 10^{-4}$ s^{-1} and (U, V) are the dimensional horizontal velocities.

3.4. Forcing and initial conditions

We impose downfront, westerly (West to East, or W–E) surface-winds that vary sinusoidally in the meridional direction (Fig. 2, bottom panel). The amplitude of the westerly wind-stress, τ_x, increases linearly from zero to its maximum value of 0.1 N m^{-2} over a day. We prescribe a south-to-north (S–N) density gradient confined to the mixed layer and in thermal-wind balance with the westerly jet, as shown in Fig. 1. The top panel of Fig. 2 shows the initial profiles of buoyancy frequency, N^2, and the potential density, ρ, at the front. The variable N^2 assumes a uniform value of 10^{-6} s^{-2} within the ML, which reaches a maximum $\approx 3 \times 10^{-4}$ s^{-2} through the pycnocline and is constant at 1.5×10^{-6} s^{-2} below the pycnocline. The middle panel in Fig. 2 shows the free-surface elevation and the meridional variation of the meridional buoyancy gradient, $\partial b/\partial y$ at a depth of 50 m, where $b = -(g/\rho_0)(\bar{\rho} - \rho_0)$ is the buoyancy. We do not maintain a constant reservoir of available potential energy (APE) but allow the S–N density gradient to vary in time. The higher elevation of the free surface on the lighter side ensures the initial barotropic and baroclinic pressure gradients at the bottom of the ML are equal and opposite. To nudge the onset of instabilities the density front has an initial wiggle in the form of a sinusoidal wave whose amplitude is 100 m and wavelength is equal to the zonal extent of the domain.

4. Results

4.1. Instantaneous fields: potential density and vertical velocity

Snapshots of the near-surface density and velocity fields after $t = 20T_f$ (Fig. 3 and 4), where $T_f = 2\pi/f_0$ is one inertial period, show the front has gone baroclinically unstable and developed meanders whose edges exhibit submesoscale features. There are
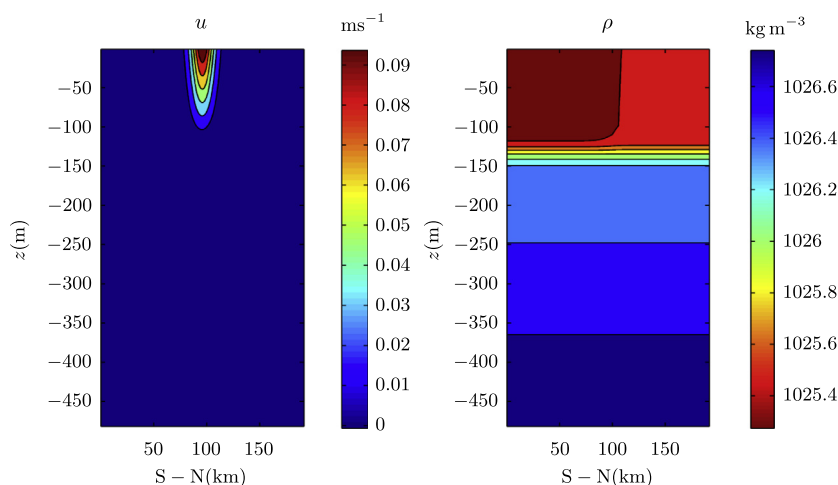

Fig. 1. The initial potential density field is in thermal-wind balance with a westerly geostrophic jet confined to the mixed layer. The level of no motion lies at $z = -105$ m, the bottom of the ML.
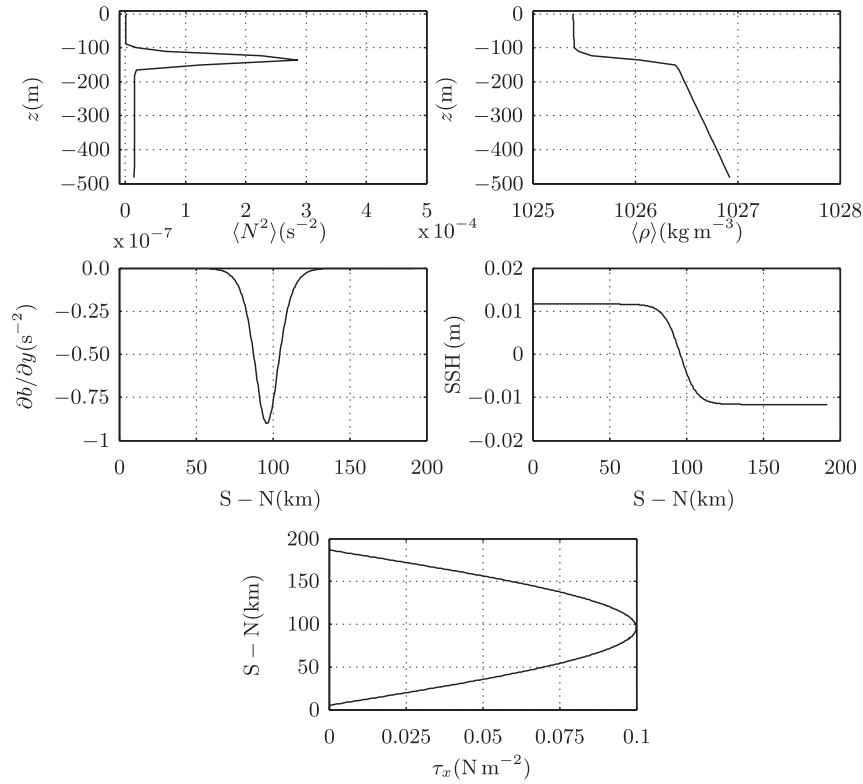
Fig. 2. Top panel: Initial vertical profiles of N^2 (s^{-2}) and ρ (kg m^{-3}) at $y = 96$ km. Middle panel: Initial meridional variation of the lateral buoyancy gradient, $\partial b/\partial y$ (s^{-2}), at a depth of 50 m and of the free-surface elevation (in m). Bottom panel: Meridional variation of zonal wind-stress (after initial ramping up), showing a sinusoidal profile with an amplitude of 0.1 N m^{-2}.
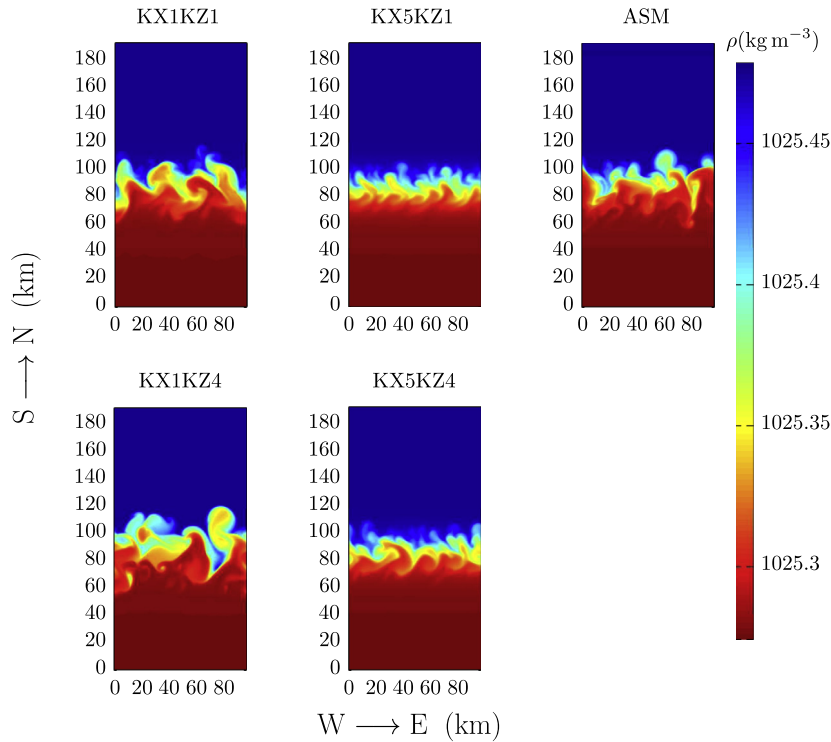

Fig. 3. Snapshots of the near-surface ($z = -10$ m) potential density field at $t = 20T_f$, where $T_f = 2\pi/f_0 = 17.5$ hours is one inertial period, for the constant-K_x and ASM simulations.
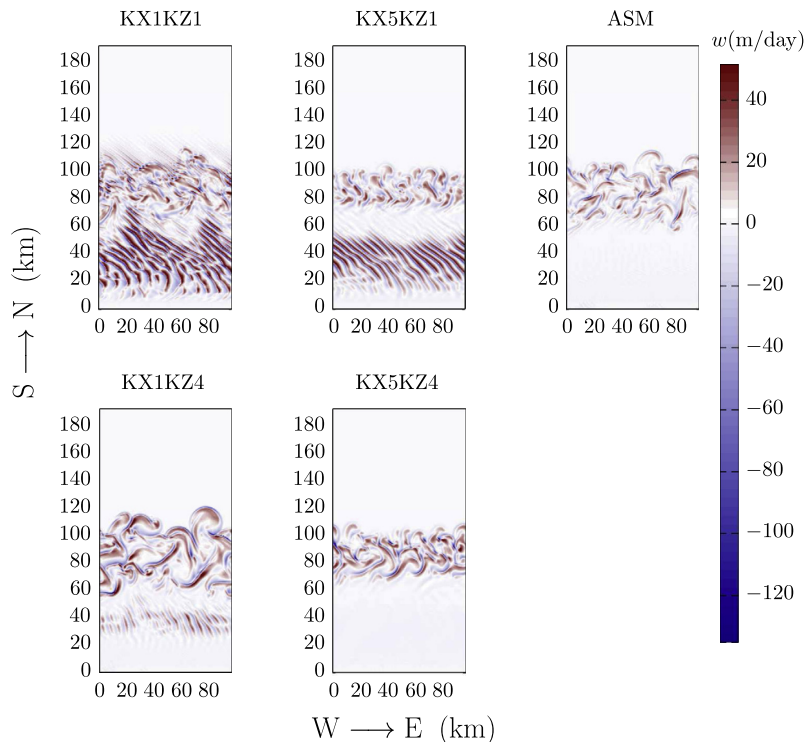
Fig. 4. Snapshots of the near-surface ($z = -10$ m) vertical velocity field at $t = 20T_f$, where $T_f = 2\pi/f_0 = 17.5$ hours is one inertial period, for the constant-K_x and ASM simulations.

noticeable differences between the various runs. Among the constant-K_x runs those with $K_x = 1$ m^2 s^{-1} exhibit more pronounced meanders and sharper frontal gradients. The meandering features are weaker for the $K_x = 5$ m^2 s^{-1} simulations, due likely to the direct influence of the lateral SGS viscosity on the instability scale (Section 3.2). The potential density field obtained using the ASM is closer to those obtained with $K_x = 1$ m^2 s^{-1} than with $K_x = 5$ m^2 s^{-1}.

The vertical velocity (Fig. 4) field from the different simulations shows marked differences of which the most prominent is the presence of wave-like features for most of the constant-K_x runs. These features are most evident for $K_x = 1$ m^2 s^{-1} but increasing K_z attenuates them and in some cases (KX5KZ4) removes them completely. The waves appear to be highly directional with a visually inferred zonal wavelength of 6–7 km. The zonally-averaged Eulerian temporal spectra of w near the front (not shown) show the frequency of the waves lies between f and $1.5f$ which raises the possibility their intrinsic frequency (without the Doppler shift) is inertial. Kunze's analysis of near-inertial motions near fronts (Kunze, 1985) showed the near-inertial wave field is strongly anisotropic and directional. His formulation, however, requires $Ro \ll 1$ whereas submesoscale eddies are characterized by $Ro \sim O(1)$ (Thomas et al., 2007) near the frontal edges. For the purposes of this study, our interest in these waves is limited to their transport of kinetic energy generated near the front. The removal of kinetic energy near a front can either occur irreversibly via a forward cascade to smaller scales or by its transport to other regions of the flow. The dominance of one of these two modes of removal of kinetic energy over the other thus hinges on the relative strengths of SGS dissipation and turbulent transport (advective and pressure fluxes). Experiments in the Kuroshio (D'Asaro et al., 2011; Nagai et al., 2012) show upper-ocean turbulent dissipation near fronts is enhanced. This would imply both local destruction via forward cascades and transport contribute to the removal of eddy kinetic energy. Fig. 4 suggests the strong levels of radiation might be an indicator of inadequate SGS dissipation. We confirm

this is indeed the case in Section 4.5 where we discuss the eddy kinetic energy (EKE) budgets and their implications for the SGS dissipation.

The signature of the potential-density field is evident in all cases except KX1KZ1. The vertical motions near the frontal edges indicate upwelling on the lighter side of the front and downwelling on the denser side, suggestive of a thermally direct circulation induced by the ML eddies (Capet et al., 2008c; Mahadevan, 2006). Downwelling is stronger than upwelling and occurs in narrower streaks of length O(10 km) and width O(1 km). For the ASM, the peak negative velocities ($\approx$120 m/day) are much larger than the peak positive velocities ($\approx$50 m/day). This asymmetry is also present in simulations with $K_x = 1$ m^2 s^{-1} and to some extent for $K_x = 5$ m^2 s^{-1}. The difference in the peak upwelling and downwelling velocities was also reported in previous studies (Capet et al., 2008c; Klein et al., 2008; Mahadevan, 2006).

Snapshots of the near-surface SGS viscosity component, K_{11}, at $t = (7, 15, 20)T_f$ (Fig. 5) reveal its horizontal structure, like that of w, is tied to that of the potential density field. The maximum values of K_{11} occur along the meandering edges of the front characterized by large strain rates. Probability density functions of K_{11} and K_{13} at $t = 20T_f$ reveal the former exhibits strong positive skewness while the latter is skewed (positively) to a much smaller extent (Fig. 6). A vertical profile of K_{11} near the front (Fig. 7) shows its largest values are O(1) m^2 s^{-1}, near the surface. A similar profile for K_{13} (Fig. 7) shows it is O(10^{-2}) m^2 s^{-1} near the surface and the base of the ML, and O(10^{-3}) m^2 s^{-1} within the middle of the ML. The high mean values of K_{13} near the base of the mixed layer are associated with zonal streaks of alternating positive and negative shear. The positive and negative shear cancel each other upon averaging zonally but contribute to K_{13} (Eq. 6).

4.2. Spectra and spectral fluxes

Near-surface zonal spectra of u and ρ for different SGS constants at $t = 15T_f$ (Fig. 8, top panel) exhibit a slope of -2
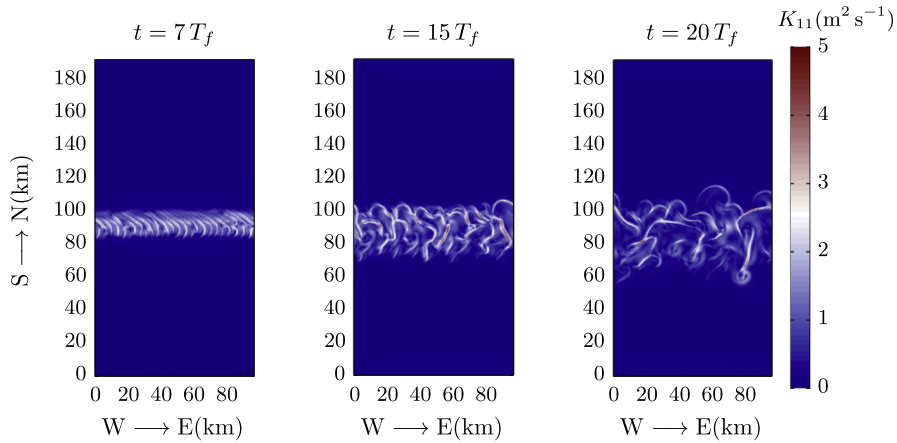
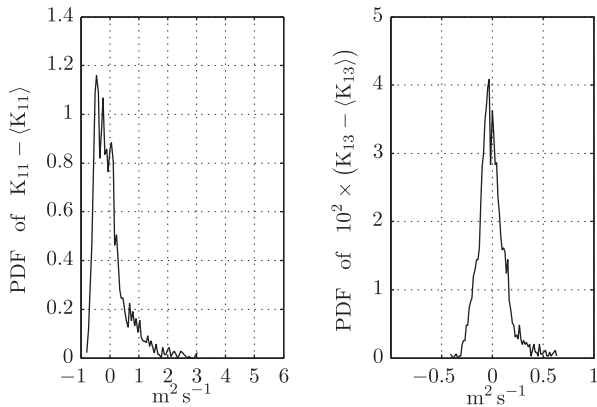**Fig. 5.** Near-surface ($z = -10$ m) evolution of K_{11}.

Fig. 6. Probability density function (PDF) of fluctuating K_{11} and $10^2 \times K_{13}$ at $z = -10$ m and $t = 20T_f$, where $T_f = 2\pi/f_0 = 17.5$ hours is one inertial period. Each PDF is constructed from a horizontal slice of data spanning the entire zonal extent of the domain and a meridional distance of 6 km centered at $y = y_f = 96$ km, the initial location of the front. The areal means of K_{13} and K_{11} are subtracted out.
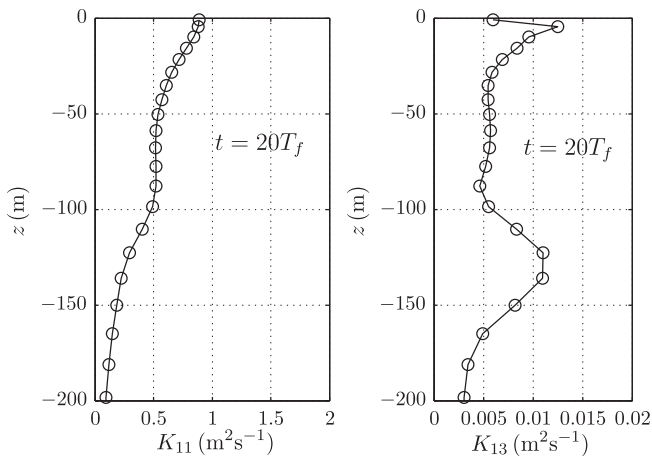

Fig. 7. Vertical profiles of K_{11} and K_{13} at $t = 20T_f$, where $T_f = 2\pi/f_0 = 17.5$ hours is one inertial period. The profiles are averaged zonally, meridionally and temporally. The meridional averaging window spans 6 km centered at $y = y_f = 96$ km, the initial location of the front. The temporal averaging occurs over one inertial period centered at $t = 20T_f$. The circles indicate the vertical grid levels.

approximately over a wavenumber range that varies with the value of the subgrid constant. For $(c_1, c_2) = (0.25, 0.25)$, this range exists for 3×10^{-4} rad m^{-1} $< \kappa_x < 10^{-3}$ rad m^{-1}, or length scales

6–20 km ($2\pi/\kappa_x$). A slope of -2 at intermediate scales is consistent with previous numerical studies (Capet et al., 2008b; Klein et al., 2008). The higher values of the SGS constants lead to increasingly steeper slopes at the high wavenumbers and a narrowing of the wavenumber range where the spectral slope is -2, a consequence of increased SGS dissipation. In none of the cases does the spectral slope of -2 extend all the way to the grid cut-off wavenumber. For that to be possible, we would require zero numerical mixing and an SGS model that achieves strict scale-separation in spectral space, i.e., it contaminates no scale larger than the grid cut-off.

We infer the direction of energy flux from the spectral flux, $\Pi(\kappa_x)$, defined as $\Pi(\kappa_x) = -\int_{\kappa_x}^{\kappa_{max}} \widehat{\mathbf{u}^*} \cdot (\mathbf{u} \cdot \widehat{\nabla})\mathbf{u}$, where $\wedge$ denotes a Fourier transform and $\mathbf{u}^*$ denotes the complex conjugate of the three-dimensional velocity vector, $\mathbf{u}$. The boundary condition $\Pi(\kappa_{max}) = 0$ is implicit in the definition of $\Pi(\kappa_x)$. At the large scales, the spectral flux is negative implying an inverse cascade of energy (Fig. 8, bottom panel). It is positive for $\kappa_x > 6 \times 10^{-4}$ rad m^{-1} (<10.5 km), indicative of a downscale transfer of energy at those scales. Capet et al., 2008b found the transition from an inverse to a forward cascade occurs at $\kappa_x \approx 3 \times 10^{-4}$ rad m^{-1}. It is essential consistency check that we resolve the onset of the forward cascade when using an SGS model that effects a forward cascade.

Unlike the velocity spectra the spectral flux changes appreciably with varying SGS constants, exhibiting a spread of nearly 50% at the large scales (low κ_x). Higher SGS dissipation results in a decrease in the strengths of both the inverse and the forward cascades. For instance, both the inverse and forward spectral fluxes for $(c_1, c_2) = (0.25, 0.50)$ are negligible.

The corresponding spectra for $K_x = 1$ m^2 s^{-1} (Fig. 9) are similar to those for the ASM in magnitude and slope. The simulations with $K_x = 5$ m^2 s^{-1} exhibit a marked decrease in spectral levels, potentially due to the high value of lateral viscosity (Section 3.2). The spectral flux for KX1KZ1 and KX1KZ4 (Fig. 9) shows an inverse cascade at the larger scales and a forward cascade for $\kappa_x > 6 \times 10^{-4}$ rad m^{-1}. For $K_x = 5$ m^2 s^{-1} both the inverse and forward cascades are diminished strongly and the spectral flux is nearly indistinguishable from zero. The inverse cascade facilitates the spatial growth of eddies that result originally from a geostrophic baroclinic instability within the mixed layer. Weak inverse cascades thus limit the spatial scale of the eddies, as is evident for KX5KZ1 and KX5KZ4 (Fig. 3). Interestingly, the spectral magnitudes and spectral fluxes are higher upon increasing the vertical SGS viscosity within the ML. This trend is clearer in the simulations with $K_x = 1$ m^2 s^{-1}. We presently lack a definitive explanation for this result but speculate the increase in the strength of the inverse cascade might be related to the effects of
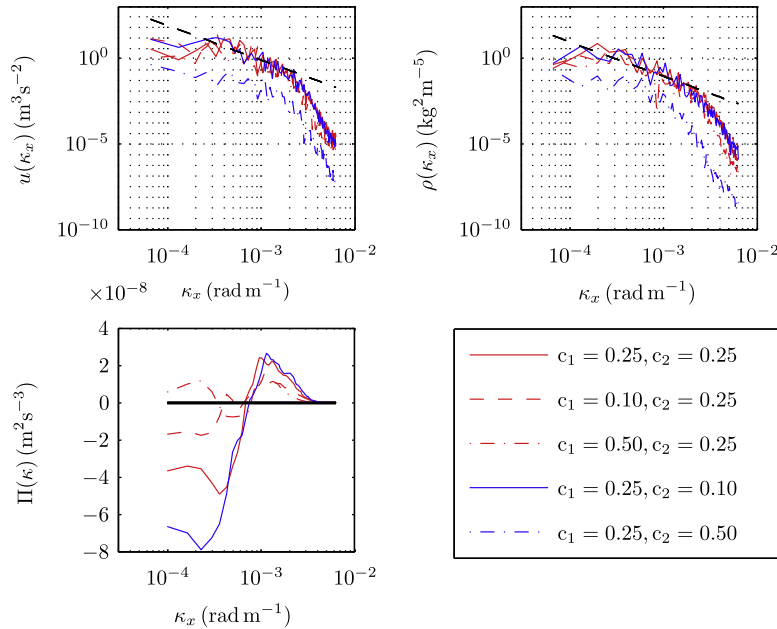
Fig. 8. Top panel: Log–log plot showing near-surface spectra (at $z = -4.5$ m) plotted versus zonal wavenumber, κ_x (rad m^{-1}), at $y = 96$ km and $t = 15T_f$, where $T_f = 2\pi/f_0 = 17.5$ hours is one inertial period. The dashed line has a slope of -2. Top left: Zonal velocity spectra, Top right: Potential density spectra. Bottom panel: Spectral flux, $\Pi(\kappa)$ (m^2 s^{-3}) plotted versus zonal wavenumber in a linear-log plot. The different curves denote different combinations of SGS constants. The spectral flux for $c_1 = 0.25, c_2 = 0.50$ (dash-dot line in blue) has much smaller magnitudes and is nearly coincident with the zero line. The spectra and spectral fluxes are averages over one inertial period centered at $t = 15T_f$. A wavenumber of 10^{-3} rad m^{-1} corresponds to a length scale of $2\pi/10^{-3}$ m, or 6.28 km. (For interpretation of the references to colour in this figure legend, the reader is referred to the web version of this article)
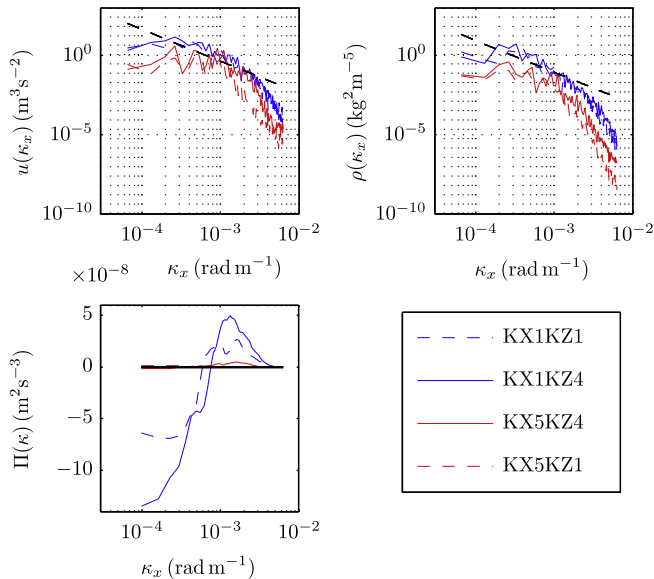

Fig. 9. Similar to Fig. 8 but for an SGS model with constant lateral SGS viscosities and an analytically prescribed vertical SGS viscosity.

friction on the triadic interactions, as described by the nonlinear advection term in spectral space. The change in the magnitude of the inverse cascade at the largest scales could possibly be a consequence of "distant" triadic interactions[8] playing a non-negligible role in determining the magnitude of the inverse cascade. The trends exhibited by the forward cascade accord with our intuition that a higher SGS dissipation must yield a greater downscale flux of energy close to the grid cutoff. The above discussion shows the combined ef-

fects of horizontal and vertical SGS mixing can be subtle even in an SGS model as bare as one using constant lateral SGS viscosities and an analytically prescribed vertical SGS viscosity. We conclude this section by noting the spectra and the spectral fluxes can exhibit considerable sensitivity to the horizontal and vertical SGS parameterizations even at scales considerably larger than the grid-cutoff. Furthermore, this sensitivity cannot always be explained trivially by merely comparing the lateral SGS viscosities.

4.3. Extraction of APE

Vertical profiles of m, the ratio of the isopycnal slope, $-\langle b_y \rangle/\langle b_z \rangle$, to the slope along which fluid parcels exchange buoyancy in the y-z plane, $\langle v'b' \rangle/\langle b'w' \rangle$, illustrate how efficiently the APE residing in the front is converted to kinetic energy (Fig. 10). The variables b_y and b_z denote the meridional and vertical buoyancy gradients, respectively. Analytical arguments predict maximum extraction of APE occurs when $m = 2$ (Eady, 1949; Haine and Marshall, 1998). In simulations of an unforced front, Fox-Kemper et al., 2008 found m settles to a value between one and two after six to seven inertial periods (assuming a Coriolis parameter of 10^{-4} rad s^{-1}). For fronts forced by downfront winds, simulations show the buoyancy fluxes eventually become aligned with the isopycnals under quasi-equilibrium conditions, where the destratification due to Ekman advection of heavier over lighter fluid counters the restratification induced by the slumping of isopycnals (Mahadevan et al., 2010).

The depths over which the APE is extracted efficiently and the orientation of the buoyancy fluxes vary in the five cases. For the ASM, there is an initial Eady phase where $m \approx 2$ over bulk of the mixed layer except near the surface. At later times the buoyancy fluxes are nearly aligned with the isopycnals and $m = 1$. The simulations with $K_x = 1$ m^2 s^{-1} yield $m = 2$ but at different times and over a range of depths smaller than does the ASM. For $K_x = 5$ m^2 s^{-1} m attains the value 2 much later than for ASM and $K_x = 1$ m^2 s^{-1}. While the efficiency of APE extraction is sensitive

---

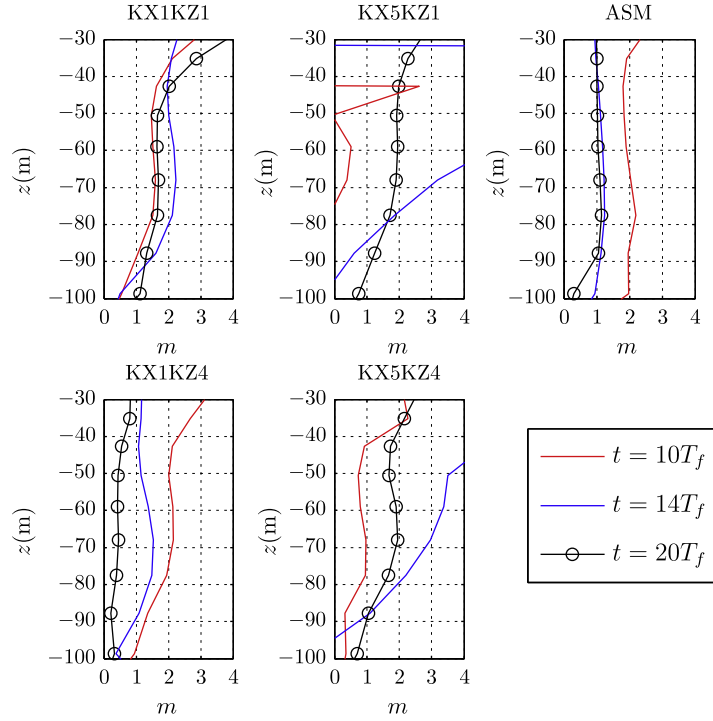[8] Interactions between modes far-removed in wavenumber space

Fig. 10. Vertical profiles of m, the ratio of the isopycnal slope, $-\langle b_y \rangle / \langle b_z \rangle$, to $\langle b'w' \rangle / \langle b'v' \rangle$, the slope along which fluid parcels exchange buoyancy in the y-z plane, at $t = (10, 14, 20)T_f$ where $T_f = 2\pi/f_0 = 17.5$ hours is one inertial period. We have averaged the profiles zonally, temporally over one inertial period and meridionally over a distance 2 km centered at $y = y_f$. For the most efficient extraction of APE, $m = 2$ (Eady, 1949; Haine and Marshall, 1998). The circles on the black curve indicate the vertical grid levels.

to both horizontal and vertical SGS mixing, it does not differ greatly between the simulations with $K_x = 1\ \text{m}^2\,\text{s}^{-1}$ and the ASM. The simulations with $K_x = 5\ \text{m}^2\,\text{s}^{-1}$ show considerably different trends, due likely to the adverse influence of the lateral SGS viscosity (Section 3.2).

4.4. SGS dissipation of buoyancy variance

The orientation of the buoyancy fluxes has implications for the SGS dissipation of the resolved-scale buoyancy fluctuations, χ. Whenever Ri exceeds $Ri_c = 0.25$ we turn off the vertical SGS diffusivity (see Section 2.2.1) and consequently, χ. From the equation for the resolved-scale buoyancy variance it follows isopycnal fluxes do not generate any buoyancy fluctuations. In the absence of external heating or cooling, cross-isopycnal buoyancy fluxes are the primary source of buoyancy fluctuations in a domain-averaged sense, assuming the divergence of advective and pressure fluxes integrate to zero (page 434; Vallis, 2006). Under quasi-equilibrium conditions we then expect production of buoyancy variance to balance SGS dissipation of the same, in a domain-averaged sense. Thus, isopycnal buoyancy fluxes, as observed at later times in some simulations, are not wholly inconsistent with near-zero SGS dissipation. We confirmed turning off the vertical SGS diffusivity yields near-zero values for χ implying the horizontal gradients of buoyancy contribute minimally to χ.

4.5. Eddy kinetic energy budget and SGS dissipation

This section examines the various terms in the zonally-averaged eddy kinetic energy (EKE) budget and explores the balance between them. We relate, where possible, magnitudes of the dominant production term in the EKE budget to existing scaling estimates in the literature.

The non-dimensional EKE budget is given by,

$$
\frac{\partial \langle u_i' u_i' \rangle}{\partial t} = \underbrace{-u_j' \frac{\partial \langle u_i' u_i' + e_{\text{sgs}} \rangle}{\partial x_j} - \langle \tilde{u}_j \rangle \frac{\partial \langle u_i' u_i' + e_{\text{sgs}} \rangle}{\partial x_j}}_{\text{Advection}}
$$

$$
\times \underbrace{-\left(u_i' u_j' \right) \left[\left. \frac{\partial \tilde{u}_i}{\partial x_j} \right|_{\text{geo}} + \left. \frac{\partial \tilde{u}_i}{\partial x_j} \right|_{\text{ageo}} \right]}_{\text{Shear production}} + \underbrace{b'w'}_{\text{Buoyancy}}
$$

$$
\times \underbrace{- \frac{1}{\rho_0} \frac{\partial \langle p' u_i' \rangle}{\partial x_i}}_{\text{Pressure transport}} + \underbrace{\tau_{ij}^d \tilde{s}_{ij}}_{\text{SGS dissipation } (\epsilon_{\text{sgs}})} , \tag{13}
$$

where the angled brackets denote zonal averaging and the primed variables are fluctuations from the corresponding zonal averages. For instance, u_i' is the deviation of $\tilde{u}_i$ from its zonal average, $\langle \tilde{u}_i \rangle$. The terms in (13) describe the different gain and loss terms that produce or destroy the kinetic energy of eddies spanning the entire range of scales resolved in our simulation. Both the resolved-scale and SGS kinetic energy contribute to the advection term but our plots do not show the subgrid contribution as we lack a parameterization for e_{sgs}.

Anisotropic Smagorinsky model. The near-surface resolved-scale eddy kinetic energy (EKE) budget (Fig. 11, left panel) shows $\epsilon_{\text{sgs}} \sim O(10^{-6})\ \text{m}^2\,\text{s}^{-3}$ and is balanced approximately by a geostrophic shear production. This balance is reminiscent of a traditional shear-driven Monin–Obukhov (MO) layer. The other terms in the budget are much smaller in comparison. MO-scaling prescribes u_* and z as the appropriate velocity and length scales within the inertial surface-layer where $u_* = \sqrt{\tau_x/\rho_0}$ is the friction velocity. Estimating $\epsilon_{\text{sgs}} \sim u_*^3/z$, where $u_* = 0.01\ \text{m s}^{-1}$ (for $\tau_x = 0.1\ \text{N m}^{-2}$) and $z \sim O(1)$ m we obtain $\epsilon_{\text{sgs}} \sim O(10^{-6})\ \text{m}^2\,\text{s}^{-3}$, which is in reasonable agreement with the near-surface values. Although the dominant production terms appear to scale on the MO variables u_* and z within this near-surface layer, it is different
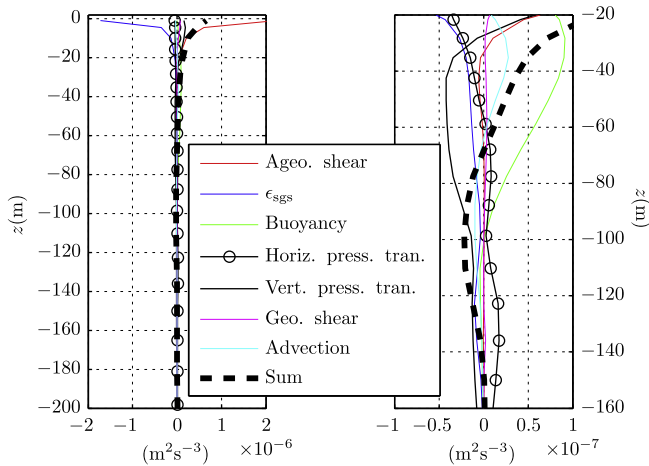
Fig. 11. Left: EKE budget with zonal, meridional (near the front) and temporal (over one inertial period) averaging, obtained using the ASM, for -100 m $< z < 0$ m at $t = 20T_f$, where $T_f = 2\pi/f_0 = 17.5$ hours is one inertial period. Right: the budget terms for -160 m $< z < -20$ m. The meridional averaging is performed over 6 km centered at the front. The range on the x-axis is different in the two plots. The circles on the lateral pressure transport profile indicate the vertical grid levels.

from the traditional MO layer because the surface buoyancy flux is zero, which should theoretically yield an infinitely deep MO layer. The finite depth of this MO-like layer even in the absence of surface buoyancy fluxes is due to Ekman advection by downfront winds, as we show later in this section.

Deeper down in the ML (-100 m $< z < -20$ m), the EKE budget is buoyancy-driven and exhibits a more complex balance (Fig. 11, right panel). The dominant term is the vertical buoyancy flux, $\langle b'w' \rangle$, whose positive sign is consistent with the notion of submesoscale eddies restratifying the flow by converting APE to kinetic energy (Fox-Kemper et al., 2008). The vertical buoyancy flux is balanced partially by a combination of vertical pressure transport, SGS dissipation and advection. The sum of all terms but the advection of SGS EKE on the right side of (13) is smaller than the dominant term in the budget but is not negligible. The SGS dissipation is smaller than the dominant production term but is of the same order of magnitude. Vertical pressure transport dominates lateral pressure transport and is the dominant loss term for -100 m $< z < -30$ m. The relative proportions of EKE destroyed locally by the subgrid model and radiated away by pressure transport depend on the subgrid constant. Increasing the subgrid constant enhances the fraction of EKE destroyed locally while decreasing the same causes more of the EKE to be radiated away.

We now attempt to justify the magnitude of the dominant production term at depths -100 m $< z < -20$ m. We begin by noting the EKE budget in Fig. 11 bears qualitative resemblance to a canonical mixed layer with no front, forced by a combination of surface winds and cooling. In such a canonical mixed layer, under quasi-equilibrium conditions there exist a shear-driven MO layer and a buoyancy-driven layer at depths greater than the MO length scale. The relative depth of these two layers will depend on the relative strengths of wind forcing and surface cooling. Our simulations have zero surface buoyant forcing, yet the shear-driven layer has a finite depth. A possible explanation is the role played by the "Ekman Buoyancy Flux" (EBF; Thomas and Taylor, 2010), an effective buoyancy flux due to Ekman advection of heavier over lighter fluid by the downfront winds. The EBF is defined as:

$$\text{EBF} = \frac{\tau_x}{\rho_0 f_0} \langle |S^2| \rangle, \tag{14}$$

where $S^2 = -b_y$. Substituting representative values $\tau_x = 0.1$ N m^{-2} and $\langle |S^2| \rangle = 0.6 \times 10^{-7}$ s^{-2} in (14), we obtain EBF $= 0.58 \times 10^{-7}$ m^2 s^{-3}. Scaling the a geostrophic shear production as u_*^3/z (from

MO scaling) we can determine an effective MO length scale, $L_{\text{MO,eff}} \sim u_*^3/\text{EBF}$, by replacing the surface buoyancy flux in the traditional definition of L_{MO} with the EBF. Substituting values, we obtain $L_{\text{MO,eff}} = 17.2$ m, which is consistent with Fig. 11. Our estimate of EBF scales $\langle b'w' \rangle$ reasonably within the ML at depths greater than $L_{\text{MO,eff}}$. To summarize, $L_{\text{MO,eff}}$ is similar to the traditional MO length scale to the extent it determines whether the EKE budget is dominated by shear (ageostrophic shear) or buoyancy (due to restratification by eddies). For the magnitudes of τ_x and $\langle S^2 \rangle$ considered here, $\langle S^2 \rangle$—through the EBF—sets the depth of the layer in which the dominant terms in the EKE budget obey MO scaling; it does not influence explicitly the magnitudes of these terms within this layer as they can be explained using the MO variables u_* and z. The situation is different in the region below the MO-like layer where the EKE budget is dominated by the buoyancy flux, whose magnitude depends explicitly on the EBF and hence, on $\langle S^2 \rangle$.

As the above scaling arguments hold only for quasi-equilibrium conditions, what follows is an evaluation of the relative strengths of: (i) destratification by Ekman advection; and (ii) restratification by ML instabilities, within the framework put forth by Mahadevan et al., 2010.

Mahadevan et al., 2010 introduced a non-dimensional parameter, $r \equiv |\psi/\psi_e| = \tau_x/(0.06\rho(MLD)^2 \langle b_y \rangle)|_{t=0}$, where ψ is the overturning stream function, ψ_e is the eddy stream function and $b_y = \partial b/\partial y$ is the meridional buoyancy gradient. The overturning stream function is defined as, $\psi = -\int_0^z \langle V \rangle \, dz = \int_0^y \langle W \rangle \, dy$, where V and W denote dimensional meridional and vertical velocities, respectively. The eddy stream function is defined as follows:

$$\psi_e = \alpha \left(\frac{-\alpha \langle v'b' \rangle \langle b_z \rangle + \alpha^{-1} \langle w'b' \rangle \langle b_y \rangle}{\langle b_y \rangle^2 + \alpha^2 \langle b_z \rangle^2} \right), \quad \alpha \ll 1. \tag{15}$$

The above form for ψ_e (Plumb and Ferrari, 2005; Cerovecki et al., 2009) generalizes earlier definitions to accommodate situations where $\bar{b}_y$ or $\bar{b}_z$ become negligibly small. In submesoscale-resolving simulations of forced fronts Mahadevan et al., 2010 showed (15) successfully parameterizes bulk of the adiabatic buoyancy flux due to restratification within the ML (Mahadevan et al., 2010).

We choose $\alpha = 10^{-3}$ following Mahadevan et al., 2010, who found (15) is insensitive to α over a range 10^{-2}–10^{-4}. The angled brackets $\langle \rangle$ denote zonal averaging. The parameter r is an indicator of the competition between destratification induced by down-front winds and restratification by the mixed layer eddies. High values of r imply the down-front winds are strong enough to prevent a net relaxation of the front by the mixed layer eddies. Low values imply downfront winds too weak to prevent net restratification by the ML eddies. For r close to unity, presumably, the two tendencies balance each other resulting in an equilibrium. Using the initial values of H and b_y, we estimate $r = 1.6$. The peak magnitudes of ψ and ψ_e (Fig. 12) are approximately equal. For the ASM, the time-evolution (Fig. 13) of ψ and ψ_e (Eq. 15) averaged over the eddying region (boxed region in Fig. 12) shows r first attains unity after approximately 15 inertial periods and continues to vary thereafter between 0.7 and 1 till the end of the simulation. Thus, invoking quasi-equilibrium in the scaling arguments above is a reasonable approximation. The wiggles in ψ are damped inertial oscillations. Within a couple of inertial periods, ψ increases rapidly to values close to 1 and eventually approaches $|\psi_{\text{wind}}| \equiv \tau_x/(\rho_0 f_0) = 0.97$ m^2 s^{-1} (Mahadevan et al., 2010). For comparison we also plot the time evolution of the eddy stream-function parameterization by Fox-Kemper et al. (2008) (Fig. 13) which increases initially as the ML deepens due to wind-driven mixing and b_y stays relatively constant. After the onset of instabilities ($\approx 5T_f$) both b_y and MLD decrease as the ML shallows due to restratification by the ML eddies, which results in a continual
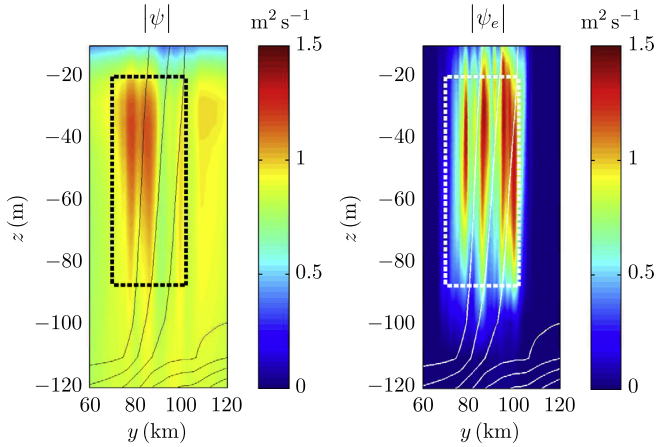
Fig. 12. ASM: Vertical sections of the magnitudes of the overturning stream function, ψ, and the eddy stream function from (15), ψ_e, at $t = 15T_f$, where $T_f = 2\pi/f_0 = 17.5$ hours is one inertial period. Solid lines are isopycnals. The box in dashed lines indicates the averaging region for Fig. 13.

decrease in the magnitude of ψ_e prescribed by the Fox-Kemper et al. (2008) parameterization.

We remark briefly on a derivation by Thomas and Taylor (2010) that shows the sum of geostrophic shear and the buoyancy flux scales on the EBF, in conditions favorable to symmetric instability. In our simulations the geostrophic shear is negligible by $t = 20T_f$ and the buoyancy flux does scales on the EBF, as noted previously. The agreement of our results with their scaling, however, is probably incidental. The derivation by Thomas and Taylor (2010) does not cover baroclinic instability, the primary instability mechanism in our simulations and our simulations are too coarse to resolve symmetric instability. Our simulations suggest a mixed-layer front forced with downfront winds (but no buoyancy) has some

similarities to a mixed layer without fronts forced by winds and buoyancy if we think of the EBF as crudely equivalent to a surface buoyancy flux. Within this context, the scaling of the buoyancy flux on the EBF at depths below the MO-like layer is less surprising. Exploring this issue further will require much higher resolution (O(10) grid points) within the shear-driven (MO-like) layer, a task beyond the scope of the present study.

$\mathbf{K}_x = 1 \text{ m}^2 \text{ s}^{-1}$. We focus only on depths greater than 20 m as the EKE budgets at shallower depths are similar for the constant-K_x and the ASM simulations. The reason for this similarity near the surface is the boundary condition $\tau_{13}^d = \tau_x/\rho_0$ at the free-surface (Section 3.3) which is imposed identically for all SGS models. This forces the SGS dissipation to balance a geostrophic shear production in the MO-like layer. Below 20 m, (Figs. 14, left panel) the nature of balance in the EKE budget differs considerably from that for the ASM (Fig. 11). The buoyancy flux remains the dominant gain term for KXKZ1 and scales approximately with the EBF. A similar scaling is observed in KX1KZ4 but both buoyancy flux and lateral pressure transport are significant gain terms. The EKE balance is also different in the two cases. In KX1KZ1 the buoyancy flux is offset almost completely by pressure transport while the balance in KX1KZ4 includes these two terms as well as a geostrophic shear. The comparable magnitudes of a geostrophic shear and buoyancy flux in KX1KZ4 make it harder to separate the ML into shear-driven and buoyancy-driven layers. The SGS dissipation in both simulations is too low and plays a negligible role in the EKE balance. Recent experimental studies in the Kuroshio (D'Asaro et al., 2011; Nagai et al., 2012) show the irreversible destruction of kinetic energy is nearly equal to the EBF, in the presence of downfront winds. We do not yet understand fully the precise level of partitioning between local destruction and radiation as routes to removal of EKE generated near the front. Nevertheless, it is reasonable to demand the SGS dissipation be at least of the same order of magnitude as the leading terms in the EKE balance, near the front. Hence, qualitatively, the EKE budgets for $K_x = 1$ are unrealistic as they predict
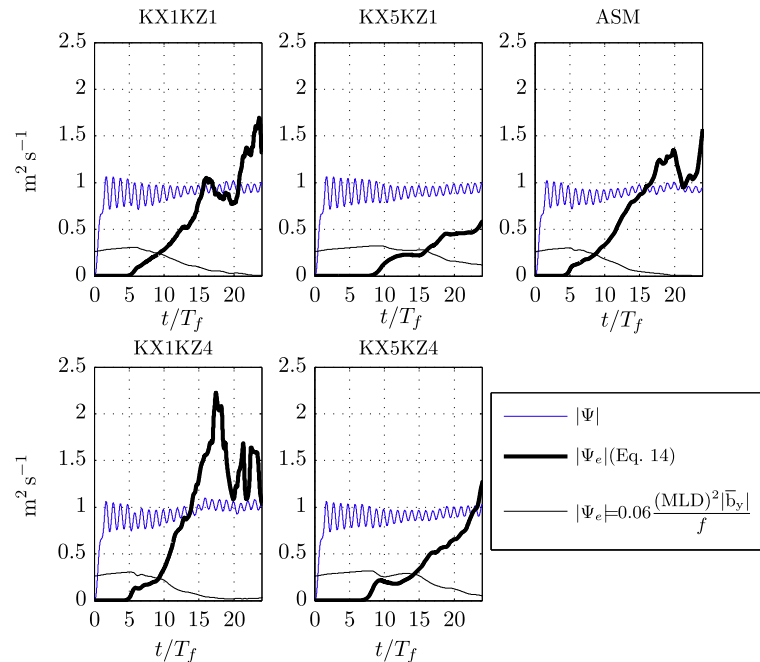

Fig. 13. Evolution of the magnitudes of the spatially averaged overturning stream function (blue solid line), ψ, and the eddy stream function (black solid lines), ψ_e, with time scaled by T_f, where $T_f = 2\pi/f_0 = 17.5$ hours is one inertial period. The ψ and ψ_e fields are averaged over the eddying region indicated by a dashed box in Fig. 12. We plot ψ_e obtained using the formulations by: (i) Cerovecki et al., 2009 (thick black solid line; Eq. 15); and (ii) $\psi_e = 0.06(\text{MLD})^2\bar{b}_y/f_0$ (thin black solid line; Fox-Kemper et al., 2008). The wiggles in ψ are inertial oscillations and the equilibrium values of ψ tend towards $|\psi_{\text{wind}}| \equiv \tau_x/(\rho_0 f_0) = 0.97 \text{ m}^2 \text{ s}^{-1}$. We estimate MLD, the mixed layer depth, as the depth where the zonally-averaged potential density is greater than its surface value by $\Delta\rho = 0.01 \text{ kg m}^{-3}$ (Brainerd and Gregg, 1995). In using the Fox-Kemper et al., 2008 parameterization we use local values of $\bar{b}_y$ (at each y and z) and the MLD (at each y) within the eddying region before averaging ψ_e over the same.
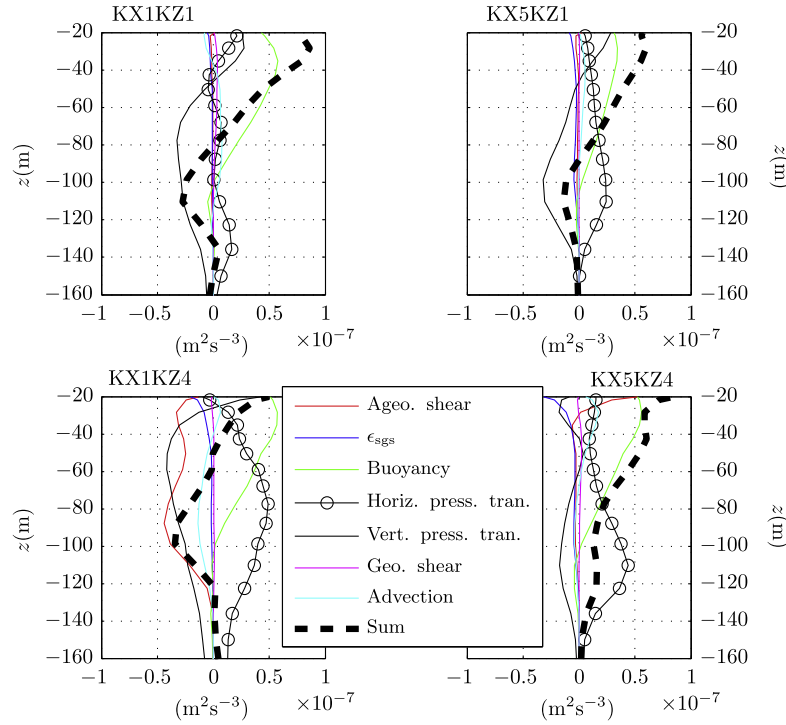
Fig. 14. EKE budgets for the non-ASM runs after zonal, meridional (near the front) and temporal (over one inertial period) averaging at $t = 20T_f$, where $T_f = 2\pi/f_0 = 17.5$ hours is one inertial period. The meridional averaging is performed over 6 km centered at the front. The circles on the black curves indicate the vertical grid levels. The near-surface balance in all four cases (not shown) is largely between a geostrophic shear and SGS dissipation.

radiation of EKE as the only available option for the removal of kinetic energy, which is consistent with the presence of the waves seen earlier in Fig. 4.

The time evolution of (ψ, ψ_e) for KX1KZ1 and KX1KZ4 are similar until $t = 15T_f$ when $r \approx 1$. Subsequently, it exhibits wider excursions for KX1KZ4 but stays below 1 for the rest of the simulation. For KX1KZ1 $r \approx 1$ between $t = 15T_f$ and $t = 20T_f$ but decreases slightly towards the end of the simulation. In both KX1KZ1 and KX1KZ4, ψ_e based on the formulation by Cerovecki et al., 2009 starts to depart from zero at $t = 5T_f$ which coincides with the onset of ML instabilities.

$\mathbf{K}_x = 5$ m^2 s^{-1}. The important gain terms in the EKE budget (Fig. 14) are buoyancy flux and lateral pressure transport. The buoyancy flux is smaller for KX5KZ1 than for any of the other simulations and does not appear to scale on the EBF. The reduced buoyancy flux is consistent with weaker restratification, a consequence of the inefficient conversion of APE to kinetic energy (Fig. 10). The SGS dissipation is higher in KX5KZ4 than in KX5KZ1 due to the increased vertical SGS viscosity. The evolution of ψ_e (thick black line, Fig. 13) shows the onset of instabilities is quicker in KX5KZ4 despite the higher SGS dissipation. Thus, a fuller appreciation of the effect of an SGS model on the resolved scales must consider both the horizontal and vertical SGS parameterizations. This is true especially when the contribution of the vertical gradients to ϵ_{sgs} dominates that from the lateral gradients, as in the present simulations (plots not shown). The value of r never attains values smaller than 1 for KX5KZ1 during the entire course of the simulation. We expect this given the highly inefficient extraction of APE which in turn, inhibits the rate of ML restratification and the growth of ψ_e (Eq. 15).

4.6. Implications of the EKE budget analysis for the SGS dissipation

The level of SGS dissipation in the EKE budgets is crucial to the ultimate fate of kinetic energy near a front. Too low a value of SGS

dissipation yields unrealistic EKE budgets with a negligible fraction of the EKE destroyed locally near the front. None of the cases tested here exhibit the opposite trend, namely, excessive local destruction with negligible transport. To return to the question posed in the introductory section regarding the appropriate level of SGS dissipation, we recommend a level of SGS dissipation that is of the same order as the leading terms in the EKE budget. Since the SGS dissipation near the surface is relatively robust to changes in the underlying SGS model, our recommendation is targeted at the buoyancy-driven layer where, for quasi-equilibrium conditions, the buoyancy flux scales on the EBF. Thus, an acceptable level of SGS dissipation in simulations where r does not differ too greatly from 1 should be of the same order of magnitude as the EBF. This estimate is useful inasmuch as the EBF can be computed easily using the wind stress and the large-scale lateral buoyancy gradient.

4.7. Skewness of $|\partial b/\partial y|$

The probability density function (PDF) of $|\partial b/\partial y|$ (Fig. 15) at approximately half the MLD reveals the various PDFs develop a negative skewness at later times in the simulation, in some cases (ASM) more prominently than others (KX1KZ4). Vertical profiles of the skewness (Fig. 16) near the front at $t = 20T_f$ show the negative values occur everywhere within the ML for all cases except KX1KZ4. One of the factors that determine the shape of the pdf of the lateral density gradient is the strength of frontogenesis by the underlying mesoscale strain field. A comparison of vertical profiles of $\mathbf{Q} \cdot \nabla_h \rho$ near the front (Fig. 17), where $\mathbf{Q} = -(\partial_x u \partial_x \rho + \partial_x v \partial_y \rho, \partial_y u \partial_x \rho + \partial_y v \partial_y \rho)$ is the "Q-vector" (Sanders and Hoskins, 1990), shows the largest values occur with the ASM while $K_x = 5$ m^2 s^{-1} yields the lowest values. Stronger frontogenesis implies greater amplification of the initial (negative) lateral buoyancy gradient which could potentially contribute to the negative skewness of its PDF. It is worthwhile to pursue the sign of the
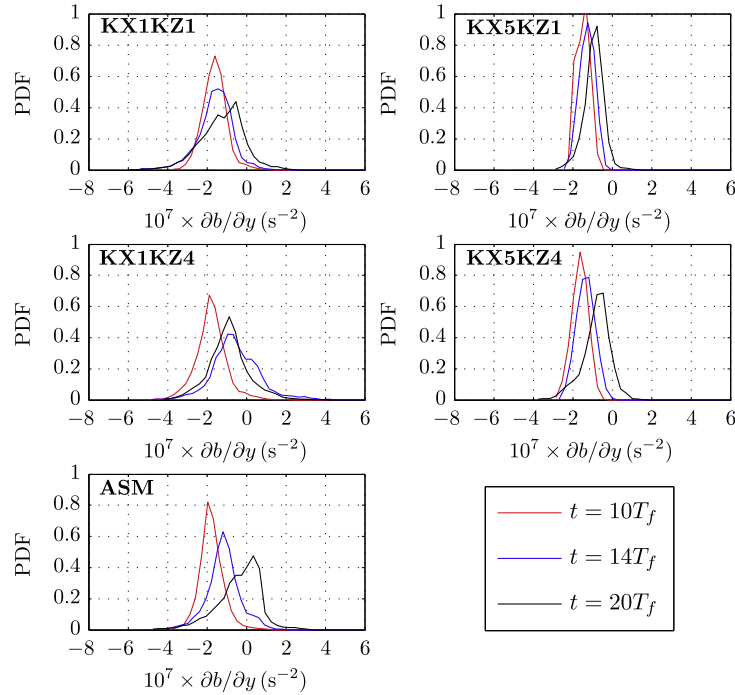
Fig. 15. Probability density function (PDF) of $10^7 \times \partial b/\partial y$ at $z = -50$ m for $t = 10T_f$, $t = 14T_f$ and $t = 20T_f$, where $T_f = 2\pi/f_0 = 17.5$ hours is one inertial period. Each PDF is constructed from a horizontal slice of data spanning the entire zonal extent of the domain and a meridional distance of 6 km centered at $y = y_f$. The PDFs are further averaged in time over one inertial period centered at the time of the snapshot.
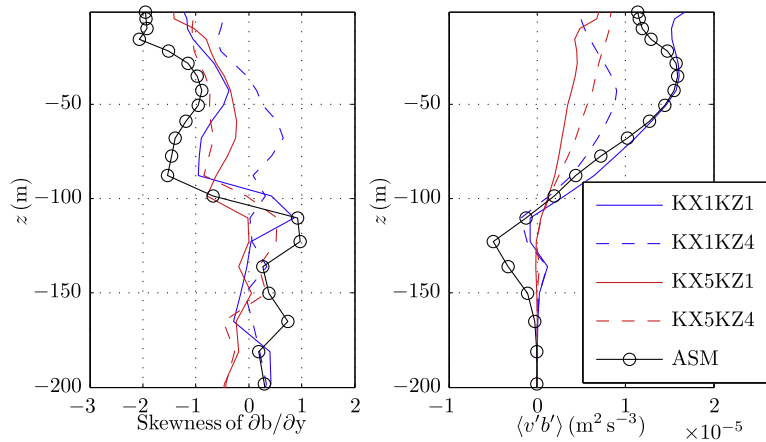

Fig. 16. Vertical profiles of: (i) the skewness of $\partial b/\partial y$; and (ii) the meridional buoyancy flux, at $t = 20T_f$, where $T_f = 2\pi/f_0 = 17.5$ hours is one inertial period. The profiles are averaged zonally, meridionally and temporally. The meridional averaging is performed across 6 km centered at $y = y_f = 96$ km, the initial location of the front. The time-averaging window spans one inertial period centered at $t = 20T_f$. The circles on the black curve indicate the vertical grid levels.

skewness further using a simple conceptual model (Thoroddsen and Atta, 1992), a description of which follows.

Consider a blob of positive buoyancy with negatively buoyant fluid beneath and above it. The buoyancy gradient immediately beneath the blob is positive and that above it is negative. In a stably stratified flow $\langle b'w' \rangle < 0$ and it is more likely the positively buoyant blob came from above than from below. During its descent, therefore, it must have undergone some mixing with negatively buoyant fluid thereby smearing out the negative buoyancy gradient in its wake. No such smearing of the positive buoyancy gradient beneath the blob occurs. The net result is a positively skewed distribution of $\partial b/\partial z$. We can enlist the above argument in toto to explain the skewness of $\partial b/\partial y$ when $\langle v'b' \rangle > 0$, as is the case within the ML in our simulations. Following the same logical sequence predicts a negative skewness for $\partial b/\partial y$. Moreover, the same arguments imply a reversal in the sign of $\langle v'b' \rangle$ must lead

to a reversal in the sign of the skewness. This is indeed the case for the ASM (Fig. 16) where the skewness of $\partial b/\partial y$ and $\langle v'b' \rangle$ reverse signs at almost the same depth. This behavior is absent in the constant K_x simulations.

4.8. Evolution of ϵ_{sgs}, $\partial b/\partial y$ and N^2

We conclude our results with time-depth plots of ϵ_{sgs}, N^2 and $|\partial b/\partial y|$ over the entire course of the simulation (Figs. 18–20) which make evident the differences in the temporal evolution of the flow for $K_x = 1$ m^2 s^{-1}, $K_x = 5$ m^2 s^{-1} and the ASM. We only show plots for KX1KZ1, KX5KZ1 and the ASM. The vertical profiles are located at the horizontal center of the domain, i.e., midway between the W–E and S–N boundaries.

The development of instabilities is slowest for KX5KZ1 (Fig. 18), as seen in the evolution of ϵ_{sgs}, which begins to attain non-negligi-
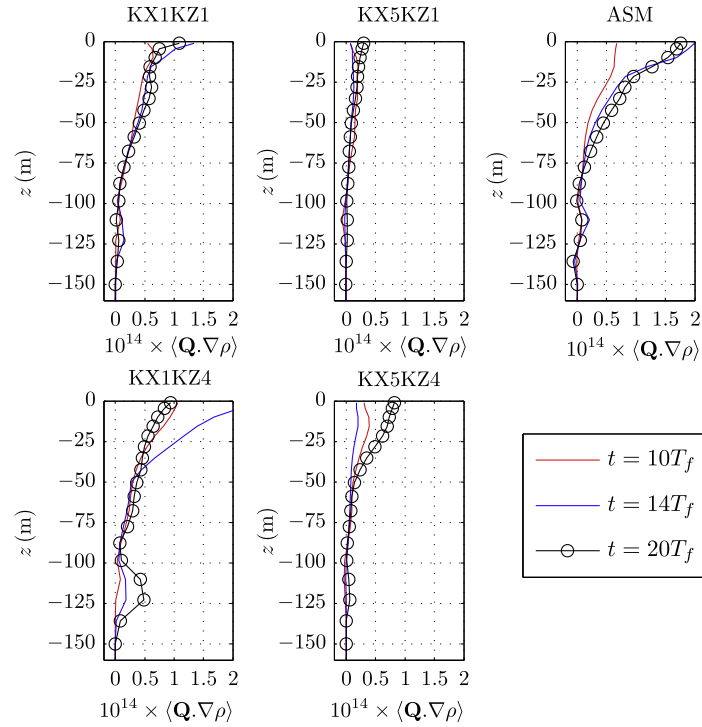
Fig. 17. Vertical profiles of zonally, meridionally and temporally averaged $10^{14} \times \mathbf{Q} \cdot \nabla \rho$ (kg^2 m^{-8} s^{-1}), where $\mathbf{Q}$ is the "Q-vector." The time-averaging window spans one inertial period (T_f) centered at the time of the snapshot, where $T_f = 2\pi/f_0 = 17.5$ hours is one inertial period. The meridional averaging is performed across 6 km centered at $y = y_f = 96$ km, the initial location of the front. The circles on the black curve indicate the vertical grid levels. (For interpretation of the references to colour in this figure legend, the reader is referred to the web version of this article)
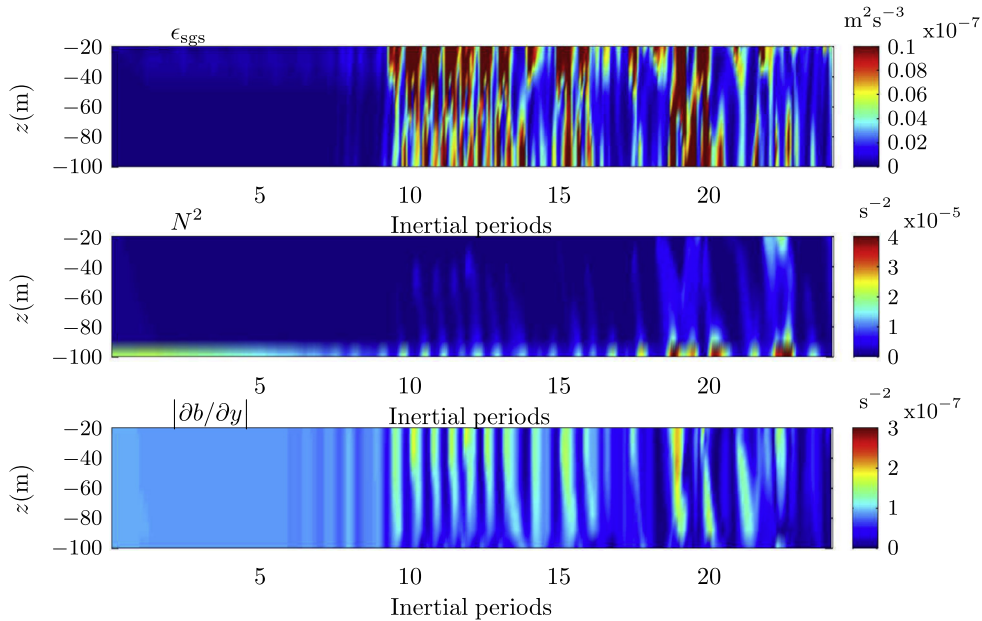

Fig. 18. $K_x = 5$ m^2 s^{-1}: A representative vertical section-plot showing the local time evolution of ϵ_{sgs}, N^2 and $|\partial b/\partial y|$ at a point midway between the W–E and S–N walls.

ble values only after 9–10 inertial periods. This is due partly to the high value of K_x (Section 3.2) but Fig. 12 suggests the effects of vertical SGS mixing are also important. The results for KX5KZ1 contrast the plots for KX1KZ1 and the ASM, where we see the presence of regions within the ML with high ϵ_{sgs} after 5–6 inertial periods. The temporal evolution of N^2 shows restratification is weakest for $K_x = 5$ m^2 s^{-1}, which is consistent with decreased

buoyancy fluxes (Fig. 14). For the ASM, maximum restratification occurs at mid-depths within the ML after $15T_f$ when ψ_e first exceeds ψ. These spots associated with strong restratification are collocated with regions of intensified $\partial b/\partial y$.

Relative to the initial peak value of $|S^2|$ ($\approx 10^{-7}$ s^{-2}), the amplification of $|S^2|$ is lesser for $K_x = 5$ m^2 s^{-1} compared to $K_x = 1$ m^2 s^{-1} and ASM. For the latter two cases, the local intensification of $|S^2|$
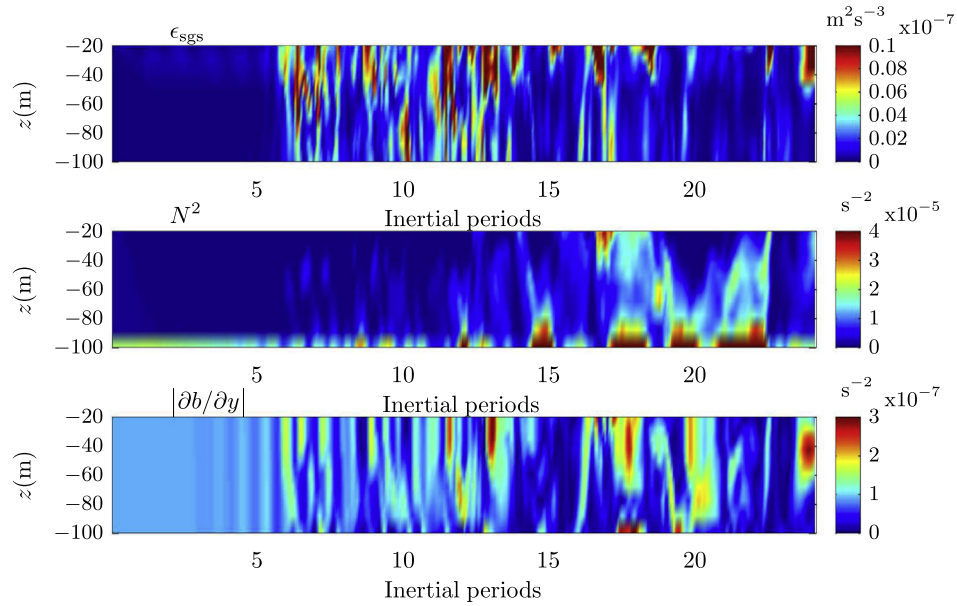
Fig. 19. $K_x = 1\ m^2\ s^{-1}$: A representative vertical section-plot showing the local time evolution of ϵ_{sgs}, N^2 and $|\partial b/\partial y|$ at a point midway between the W–E and S–N walls.
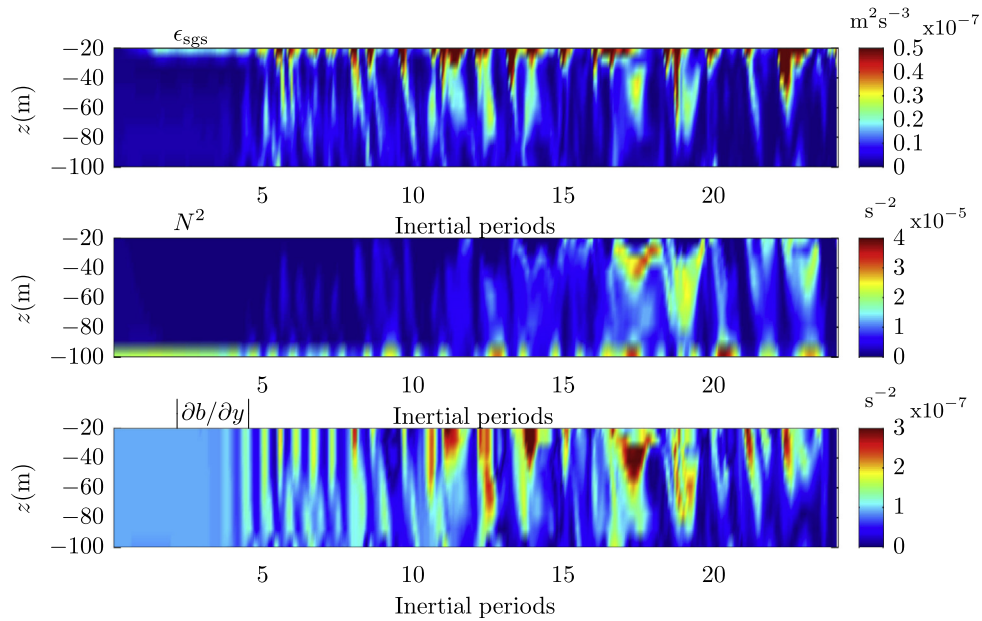

Fig. 20. ASM: A representative vertical section-plot showing the local time evolution of ϵ_{sgs}, N^2 and $|\partial b/\partial y|$ at a point midway between the W–E and S–N walls. The range on the ϵ_{sgs} colour bar differs from those in Figs. 18,19.

occurs at both shallow depths and deeper down in the ML, in some cases enhancing $|S^2|$ to three times its initial value ($0.9 \times 10^{-7}\ s^{-2}$).

5. Summary

The motivations behind this study are twofold: (i) to estimate what is a physically meaningful level of subgrid dissipation in simulations where the grid cutoff resolves part of the submesoscale (O(1–10) km) spectrum; and (ii) to explore the sensitivity of the resolved-scale features in such simulations to the level of subgrid-scale dissipation. Previous studies show the transition from an inverse to a forward cascade at the submesoscales which

suggests submesoscale-resolving simulations might permit the use of LES-based subgrid models, most of which are designed to ensure a forward cascade of energy from the resolved to the subgrid scales. Accordingly, the two subgrid closures we choose are: (i) an LES-based closure: an anisotropic Smagorinsky model developed specifically for computational grids where the horizontal resolution is much coarser than the vertical resolution (Roman et al., 2010); and (ii) a non-LES closure that uses constant lateral SGS viscosities and an analytically prescribed background vertical SGS viscosity. The anisotropic Smagorinsky model (or ASM) prescribes both lateral and vertical SGS viscosities as functions of the resolved-scale strain rate and the grid spacing.

Our problem of choice is a mixed-layer density front forced by downfront winds. Guided by past studies (Mahadevan et al., 2010), we prescribe simulation parameters that yield quasi-equilibrium conditions. To estimate the appropriate subgrid dissipation we analyze the balance between the different terms in the eddy kinetic energy budget. From the budget analysis, we identify two distinct layers within the ML: (i) a shear-driven layer near the surface; and (ii) a buoyancy-driven layer deeper down. The shear-driven layer is similar to a traditional Monin–Obukhov layer in that the dominant production and destruction terms are a geostrophic shear and subgrid dissipation, respectively, both of which scale on the surface-layer parameters u_* and z. We observe this balance in all the simulations. The depth of this shear-driven layer is determined by the Ekman buoyancy flux. Below the shear-driven layer, all simulations predict the dominant gain term in the budget is the buoyancy flux, which in most cases, scales on the Ekman buoyancy flux. The behavior of the other terms in the energy budget, however, varies considerably among the different simulations. For constant K_x, the subgrid dissipation does not enter the balance due to its low magnitude. As a result, these simulations predict the buoyancy flux is offset almost solely by pressure transport. Physically, this means the constant K_x simulations predict much of the energy generated near the front is radiated with very little of it destroyed locally via subgrid dissipation, whereas measurements show enhanced dissipation levels (D'Asaro et al., 2011; Nagai et al., 2012) near fronts. With the anisotropic Smagorinsky model the balance involves multiple terms: buoyant production, pressure transport, advection and subgrid dissipation. The magnitude of buoyant production in this layer scales on the Ekman buoyancy flux. The subgrid dissipation is smaller in magnitude than the buoyancy flux but is of the same order of magnitude and hence, contributes to the energy balance. Based on these findings we recommend a level of subgrid dissipation of the kinetic energy that is of the same order as the EBF in submesoscale-resolving simulations. This recommendation holds only for quasi-equilibrium conditions. The subgrid dissipation of potential density variance appears to be less important due to negligible production of the same at quasi-equilibrium conditions. This is consistent with the use of a subgrid-scale model in the momentum equation alone, a practice previous studies have adopted (Fox-Kemper et al., 2008; Ozgokmen et al., 2009).

The temporal and spatial evolution of the submesocale instabilities display considerable variability among the different simulations. The simulations with $K_x = 5 \text{ m}^2 \text{ s}^{-1}$ are associated with slower onset of instabilities, inefficient extraction of available potential energy, weakened cascades (inverse and forward) and negligible frontogenesis. These features are reproduced more realistically in simulations with $K_x = 1 \text{ m}^2 \text{ s}^{-1}$ or the ASM. The considerably different results for $K_x = 5 \text{ m}^2 \text{ s}^{-1}$ results are attributable partly to the adverse influence of the lateral viscosity on the instability scale, suggesting $K_x = 5 \text{ m}^2 \text{ s}^{-1}$ might be too high a value for the lateral SGS viscosity. This reasoning, however, ignores the role of vertical SGS mixing. Indeed, we observe non-trivial variability among simulations with the same value of K_x but different vertical SGS viscosities.

We conclude the parameterization of subgrid mixing can have important consequences for the evolution of submesoscale instabilities in simulations where the grid spacing resolves the submesoscales. Our results show developing better subgrid models for such simulations will require consideration of lateral and vertical subgrid mixing in concert. Finally, we have shown the use of LES-based closures is consistent with submesoscale-resolving simulations provided the grid is fine enough to resolve the onset of the forward cascade.

In this study, we have focused on the level of subgrid dissipation and not on how it is achieved. Further work is required to determine whether different subgrid-scale models yield different resolved-scale statistics for the same level of subgrid dissipation. Insights gained from analyzing the eddy kinetic energy budgets in submesoscale-resolving simulations for a wider variety of forcing conditions than those considered in this study will be useful in developing subgrid closures.

References

Boccaletti, G., Ferrari, R., Fox-Kemper, B., 2007. Mixed layer instabilities and restratification. J. Phys. Oceanograph. 37, 2228–2250.
Brainerd, K.E., Gregg, M.C., 1995. Surface mixed and mixing layer depths. Deep Sea Res. 42, 1521–1543.
Capet, X., McWilliams, J.C., Molemaker, M.J., Shchepetkin, A.F., 2008a. Mesoscale to submesoscale transition in the California current system. Part II: Frontal processes. J. Phys. Oceanograph. 38, 44–64.
Capet, X., McWilliams, J.C., Molemaker, M.J., Shchepetkin, A.F., 2008b. Mesoscale to submesoscale transition in the California current system. Part III: Energy balance and flux. J. Phys. Oceanograph. 38, 2256–2269.
Capet, X., McWilliams, J.C., Molemaker, M.J., Shchepetkin, A.F., 2008c. Mesoscale to submesoscale transition in the California current system. Part I: Flow structure, eddy flux and observational tests. J. Phys. Oceanograph. 38, 29–43.
Cerovecki, I., Plumb, R.A., Heres, W., 2009. Eddy transport and mixing on a wind- and buoyancy-driven jet on the sphere. J. Phys. Oceanograph. 39, 1133–1149.
Charney, J., 1971. Geostrophic turbulence. J. Atmosp. Sci. 28, 1087–1095.
Corrsin, S., 1951. On the spectrum of isotropic temperature fluctuations in isotropic turbulence. J. Appl. Phys. 22, 469–473.
Cottet, G.H., Wray, A.A., 1997. Anisotropic grid-based formulas for subgrid-scale models, Annual Research Briefs, Center for Turbulence Research, Stanford, CA, United States, pp. 113–122.
D'Asaro, E., Lee, C., Rainville, L., Harcourt, R., Thomas, L., 2011. Anisotropy and coherent structures in planetary turbulence. Science 332, 318–322.
Eady, E.T., 1949. Long waves and cyclone waves. Tellus 1, 33–52.
Fox-Kemper, B., Menemenlis, D., 2008. Can large-eddy simulation techniques improve mesoscale-rich ocean models? In: Hecht, M., Hasume, H. (Eds.), Ocean Modeling in an Eddying Regime, Geophysical Monograph, 177. American Geophysical Union, pp. 319–338.
Fox-Kemper, B., Ferrari, R., Hallberg, R.W., 2008. Parameterization of mixed layer eddies. Part I: Theory and diagnosis. J. Phys. Oceanograph. 38, 1145–1165.
Germano, M., Piomelli, U., Moin, P., Cabot, W.H., 1991. A dynamic subgrid-scale eddy viscosity model. Phys. Fluids 3, 1760–1765.
Haine, T.W.N., Marshall, J., 1998. Gravitational, symmetric and baroclinic instability of the ocean mixed layer. J. Phys. Oceanograph. 28, 634–658.
Harcourt, R.R., D'Asaro, E.A., 2008. Large-eddy simulation of Langmuir turbulence in pure wind seas. J. Phys. Oceanograph. 38, 1542–1562.
Kamenkovich, V.M., 1977. Fundamentals of Ocean Dynamics. Elsevier, pp. 408.
Klein, P., Hua, B.L., Lapeyre, G., Capet, X., Gentil, S.L., Sasaki, H., 2008. Upper ocean turbulence from high-resolution 3D simulations. J. Phys. Oceanograph. 38, 1748–1763.
Kunze, E., 1985. Near-inertial wave propagation in geostrophic shear. J. Phys. Oceanograph. 15, 544–565.
Large, W., McWilliams, J., Doney, S., 1994. Oceanic vertical mixing: a review and a model with a nonlocal boundary layer parameterization. Rev. Geophys. 32, 363–403.
Launder, B.E., Reece, G.J.R., Rodi, W., 1975. Progress in the development of a Reynolds-stress turbulence closure. J. Fluid Mech. 68, 537–566.
Leonard, A., 1974. Energy cascade in large-eddy simulation of turbulent fluid flows. Adv. Geophys. 18, 237–248.
Leonard, B.P., 1988. Simple high-accuracy resolution program for convective modelling of discontinuities. Int. J. Numer. Methods Fluids 8, 1291–1318.
Lévi, M., Klein, P., Treguier, A.M., 2001. Impacts of sub-mesoscale physics on production and subduction of phytoplankton in an oligotrophic regime. J. Marine Res. 59, 535–565.
Lilly, D.K., 1967. The representation of small-scale turbulence in numerical experiments. In: Proceedings of IBM Scientific Computing Symposium on Environmental Sciences, Thomas J. Watson Research Center, IBM, Yorktown Heights, NY, pp. 195–210.
Lilly, D.K., 1992. A proposed modification of the Germano subgrid scale closure method. Phys. Fluids 4, 633–635.

Mahadevan, A., 1996. A non-hydrostatic mesoscale ocean model 1: well-posedness and scaling. J. Phys. Oceanograph. 26, 1168–1880.

Mahadevan, A., 2006. Modeling vertical motion at ocean fronts. Ocean Modell. 14, 222–240.

Mahadevan, A., Archer, D., 2000. Modeling the impact of fronts and mesoscale circulation on the nutrient supply and biogeochemistry of the upper ocean. J. Phys. Oceanograph. 105, 1209–1225.

Mahadevan, A., Tandon, A., 2006. An analysis of mechanisms for submesoscale vertical motion at ocean fronts. Ocean Modell. 14, 241–256.

Mahadevan, A., Tandon, A., Ferrari, R., 2010. Rapid changes in mixed layer stratification driven by submesoscale instabilities and winds. J. Geophys. Res. 115, 1–12.

Marchesiello, P., Capet, X., Menkes, C., Kennan, S.C., 2011. Submesoscale dynamics in tropical instability waves. Ocean Modell. 39, 31–46.

McWilliams, J.C., 2003. Diagnostic force balance and its limits. Nonlinear Processes in Geophysical Fluid Dynamics. Kluwer Academic Publishers, pp. 287–304.

McWilliams, J.C., Weiss, J.B., Yavneh, I., 1994. Anisotropy and coherent structures in planetary turbulence. Science 264, 410–413.

Miles, J., 1994. On transversely isotropic eddy viscosity. J. Phys. Oceanograph. 24, 1077–1079.

Moeng, C.H., Wyngaard, J.C., 1988. Spectral analysis of large eddy simulations of the convective boundary layer. J. Atmos. Sci. 45, 3573–3587.

Molemaker, M.J., McWilliams, J.C., 2005. Baroclinic instability and loss of balance. J. Phys. Oceanograph. 35, 1505–1517.

Molemaker, M.J., McWilliams, J.C., Capet, X., 2010. Balanced and unbalanced routes to dissipation in an equilibrated Eady flow. J. Fluid Mech. 654, 35–63.

Muller, P., McWilliams, J.C., Molemaker, M., 2005. Routes to dissipation in the ocean: the 2d/3d turbulence conundrum. In: Baumert, H., Simpson, J., Sundermann, J. (Eds.), . Marine turbulence: theories, observations and models. Cambridge University Press, pp. 397–405.

Nagai, T., Tandon, A., Yamazaki, H., Doubell, M.J., 2012. Direct observations of microscale turbulence and thermohaline structure in the Kuroshio front. J. Geophys. Res. 117, 1–21.

Ohya, Y., Nakamura, R., Uchida, T., 2008. Intermittent bursting of turbulence in a stable boundary layer with low-level jet. Boundary-Layer Meteorol. 126, 349–363.

Ozgokmen, T., Iliescu, T., Fischer, P.F., Srinivasan, A., Duan, J., 2007. Large eddy simulation of stratified mixing in two-dimensional dam-break problem in a rectangular enclosed domain. Ocean Modell. 16, 106–140.

Ozgokmen, T., Iliescu, T., Fischer, P.F., 2009. Reynolds number dependence of mixing in a lock-exchange system from direct numerical and large eddy simulations. Ocean Modell. 30, 190–206.

Ozgokmen, T., Poje, A.C., Fischer, P.F., Haza, A.C., 2011. Large-eddy simulations of mixed layer instabilities and sampling strategies. Ocean Modell. 39, 311–331.

Pedlosky, J., 1987. Geophysical Fluid Dynamics, second ed. Springer, Berlin.

Perot, J.B., Gadebusch, J., 2009. A stress transport equation model for simulating turbulence at any mesh resolution. Theor. Comput. Fluid Dyn. 23, 271–286.

Piomelli, U., Cabot, W.H., Moin, P., Lee, S., 1991. Subgrid-scale backscatter in turbulent and transitional flows. Phys. Fluids 3, 1766–1771.

Plumb, R.A., Ferrari, R., 2005. Transformed Eulerian-mean theory. Part I: Nonquasigeostrophic theory for eddies on a zonal-mean flow. J. Phys. Oceanograph. 35, 165–174.

Pope, S.J., 2000. Turbulent Flows, third ed. Cambridge University Press.

Reynolds, W.C., 1990. The Potential and Limitations of Direct and Large Eddy Simulations. In: Lumley, J.L. (Ed.), . Whither Turbulence: Turbulence at The Crossroads. Springer, New York, pp. 313–315.

Roman, F., Stipcich, G., Armenio, V., Inghilesi, R., Corsini, S., 2010. Large eddy simulation of mixing in coastal areas. Int. J. Heat Fluid Flow 31, 327–341.

Sanders, F., Hoskins, B.J., 1990. An easy method for estimation of Q-vectors from weather maps. Weather Forecast. 5, 346–353.

Scotti, A., Meneveau, C., 1993. Generalized Smagorinsky model for anisotropic grids. Phys. Fluids 5, 2306–2308.

Skyllingstad, E.D., Samelson, R.M., 2012. Baroclinic frontal instabilities and turbulent mixing in the surface boundary layer. Part I: Unforced simulations. J. Phys. Oceanograph. 42, 1701–1716.

Smagorinsky, J., 1963. General Circulation experiments with the primitive equations I. The basic experiment. Mon. Weather Rev. 91, 99–164.

Spalart, P.R., 2009. Detached-eddy simulation. Ann. Rev. Fluid Mech. 41, 181–202.

Spalart, P.R., Jou, W.H., Strelets, M., Allmaras, S.R., 1997. Comments on the feasibility of LES for wings, and on a hybrid RANS/LES approach, In: Advances in DNS/LES, Proceedings of 1st AFOSR International conference on DNS and LES, Greyden Press, NY.

Speziale, C.G., 1998. Turbulence modelling for time-dependent RANS and VLES: a review. Amer. Inst. Aeronaut. Astronaut. J. 36, 173–184.

Stone, P.H., 1970. On non-geostrophic baroclinic stability: Part II. J. Atmos. Sci. 27, 721–726.

Sullivan, P.P., McWilliams, J.C., Moeng, C., 1994. A subgrid-scale model for large-eddy simulation of planetary boundary-layer flows. Boundary-Layer Meteorol. 71, 247–276.

Sullivan, P.P., Horst, T.W., Lenschow, D.H., Moeng, C., Weil, J.C., 2003. Structure of subfilter-scale fluxes in the atmospheric surface layer with application to large-eddy simulation modelling. J. Fluid Mech. 482, 101–139.

Sullivan, P.P., Mcwilliams, J.C., Melville, W.K., 2007. Surface gravity wave effects in the oceanic boundary layer: large-eddy simulation with vortex force and stochastic breakers. J. Fluid Mech. 593, 405–452.

Tandon, A., Garrett, C., 1994. Mixed layer restratification due to a horizontal density gradient. J. Phys. Oceanograph. 24, 1419–1424.

Taylor, J.R., Ferrari, R., 2009. On the equilibration of a symmetrically unstable front via a secondary shear instability. J. Fluid Mech. 622, 103–113.

Taylor, J.R., Ferrari, R., 2010. Buoyancy and wind-driven convection at mixed layer density fronts. J. Phys. Oceanograph. 40, 1222–1242.

Tejada-Martínez, A.E., 2009. A hybrid spectral/finite-difference large-eddy simulator of turbulent processes in the upper ocean. Ocean Modell. 30, 115–142.

Tennekes, H., Lumley, J.L., 1972. A First Course in Turbulence. The MIT Press, pp. 300.

Thomas, L., 2005. Destruction of potential vorticity by winds. J. Phys. Oceanograph. 35, 2457–2466.

Thomas, L.N., Taylor, J.R., 2010. Reduction of the usable wind-work on the general circulation by forced symmetric instability. Geophys. Res. Lett. 37, 1–5.

Thomas, L., Tandon, A., Mahadevan, A., 2007. Submesoscale ocean processes and dynamics. In: Hecht, M., Hasume, H. (Eds.), Ocean Modeling in an Eddying Regime, Geophysical Monograph, 177. American Geophysical Union, pp. 217–228.

Thoroddsen, S.T., Atta, C.W.V., 1992. Exponential tails and skewness of density-gradient probability density functions in stably stratified turbulence. J. Fluid Mech. 244, 547–566.

Vallis, G., 2006. Atmospheric and Oceanic Fluid Dynamics,, Cambridge University Press, pp. 745.

Wajsowicz, R.C., 1993. A consistent formulation of the anisotropic stress tensor for use in models of the large-scale ocean circulation. J. Comput. Phys. 105, 333–338.

Wyngaard, J.C., 2004. Towards numerical modelling in the "terra incognita". J. Atmos. Sci. 61, 1816–1826.